



Article

Integration of SiC Devices and High-Frequency Transformer for High-Power Renewable Energy Applications

Weichong Yao ¹, Junwei Lu ^{1,*}, Foad Taghizadeh ², Feifei Bai ¹ and Andrew Seagar ¹¹ School of Engineering and Built Environment, Griffith University, Brisbane, QLD 4111, Australia² School of Engineering, Macquarie University, Sydney, NSW 2109, Australia

* Correspondence: j.lu@griffith.edu.au

Abstract: This paper presents a novel structure of Integrated SiC MOSFETs with a high-frequency transformer (I-SiC-HFT) for various high-power isolated DC–DC converters. Several resonant converters are considered for integration in this paper, including the phase-shift full-bridge (PSFB) converter, inductor–inductor–capacitor (LLC) resonant converter, bidirectional PSFB converter, and capacitor–inductor–inductor–capacitor (CLLC) resonant converter. The applications of I-SiC-HFT are focused on V2G EV battery charging systems, energy storage in DC and AC microgrids, and renewable energy systems. SiC devices, including MOSFETs, Schottky diodes, and MOSFET modules, are used in this novel structure of I-SiC-HFT. The high-frequency magnetic structure uses distributed ferrite cores to form a large central space to accommodate SiC devices. The optimized architecture of I-SiC-HFT and heatsink structure is proposed for thermal management of SiC devices. To prove the concept, a small-scale 1.5 kW prototype I-SiC-HFT is used to demonstrate the basic structure and various performance indicators through the FEM based electromagnetic simulation and DC–DC converter experiments.

Keywords: high-frequency magnetics; high-power high-frequency transformers; full-bridge isolated DC–DC converters; SiC MOSFET



Citation: Yao, W.; Lu, J.; Taghizadeh, F.; Bai, F.; Seagar, A. Integration of SiC Devices and High-Frequency Transformer for High-Power Renewable Energy Applications. *Energies* **2023**, *16*, 1538. <https://doi.org/10.3390/en16031538>

Academic Editor: Pawel Rozga

Received: 15 December 2022

Revised: 26 January 2023

Accepted: 27 January 2023

Published: 3 February 2023



Copyright: © 2023 by the authors. Licensee MDPI, Basel, Switzerland. This article is an open access article distributed under the terms and conditions of the Creative Commons Attribution (CC BY) license (<https://creativecommons.org/licenses/by/4.0/>).

1. Introduction

Various types of magnetically isolated power converters have been extensively used in DC power supplies, such as server power supply and uninterrupted power supply (UPS), solid-state transformers (SSTs), power routers, battery energy storage, and electric vehicle (EV) charging systems. Phase-shift full-bridge (PSFB) converters and full-bridge LLC (FB-LLC) resonant converters are the most popular topologies for isolated DC–DC power converters used in those applications [1–5], where a high-frequency (HF) transformer as a magnetic isolation component is always required.

Currently, IGBT devices dominate the high-voltage (HV) and high-power (HP) applications in renewable energy systems (e.g., solar farms and wind farms), electrifications, EV motor drives, and EV charging systems. However, because the switching frequency of IGBT is limited to 20 kHz, the size of DC–DC power converters with galvanically isolated transformers is still bulky and heavy; the cost and power loss are also high. At the same time, the conventional magnetic structures and materials of HF transformers used for IGBT-based DC–DC power converters cannot take advantages of SiC MOSFETs and fully use advanced control technologies.

The HF magnetic devices using soft ferrites and amorphous alloy materials have some limitations in their operating frequency, magnetic core size, and magnetic saturation flux density. The commercially available conventional HF transformer magnetic cores and transformer structures are not the most well suited for HP HF transformers because of manufacturers' production limitations and constraints. The maximum power rating of a single HF transformer is normally limited to around 20 kW [6–8]. However, the transformer-less DC–AC inverters or DC–DC converters can be made for rated power of more than

30 kW, and a single module can be rated up to a few hundred kilowatts if SiC modular devices are used [9]. Advanced SiC MOSFETs cannot be fully used for HP and HV DC–DC converters with HF transformers because of the size limitations of soft magnetic ferrites and amorphous alloys. Therefore, the application of SiC MOSFETs in an isolated DC–DC converter is limited by the power rating of the HF transformer and its magnetic properties.

In recent years, HF, HV, and HP SiC semiconductor devices became available for various DC power supplies, DC–DC converters, and DC–AC inverters utilised in smart solid-state transformers, EV charging systems, and renewable energy systems. Since discrete SiC MOSFETs (voltage up to 1700 V, current up to 120 A) and modular SiC MOSFETs (voltage up to 1700 V, current up to 760 A) can be practically operated up to the switching frequency of about 300 kHz for HV and HP applications [10–12], it is possible to significantly reduce the size and weight reduction of galvanically isolated DC–DC power converters; power loss and other performances can also be improved. Various SiC MOSFET-based evaluation products for EV on-board chargers using isolated PSFB converters and FB-LLC resonant converters as well as vehicle-to-grid (V2G) technology using bidirectional full-bridge CLLC (FB-CLLC) resonant converters and bidirectional PSFB converters are commercially available from semiconductor manufacturers, such as Wolfspeed [13], Infineon [14], Texas Instruments [15], and so forth.

This paper is focused on the integration of SiC semiconductor devices and HP/HF transformers for full-bridge unidirectional and bidirectional DC–DC converters used in renewable energy systems and EV charging systems. Discrete integrated SiC-device high-frequency transformers (I-SiC-HFTs) can be utilized for low-voltage, low-to-medium-power (7–22 kW), vehicle-to-home (V2H) technology, and 750 V to 1000 V medium-power (MP) and HP (50–500 kW) V2G EV fast and ultra-fast chargers. Modular I-SiC-HFTs can be applied for 750 V to 1000V HP (megawatt level) V2G EV fast and ultra-fast charging stations/systems, 600 V to 1000V HP (2–18 MW) onshore and offshore wind turbines, and medium-voltage HP (megawatt to gigawatt level) solid-state transformers. In Section 2, isolated DC–DC power converters using SiC devices and their general operations are presented. The architecture of an I-SiC-HFT is proposed in Section 3, and the design, simulation, implementation, and experimental results of the I-SiC-HFT are presented in Section 4. Finally, conclusions are given in Section 5.

2. Isolated DC–DC Power Converters Using SiC Devices

The design considerations of HP HF isolated DC–DC power converters can be divided into four major directions: power electronic circuit topology, magnetic component, converter control, and thermal management. HP HF DC–DC converters with I-SiC-HFT can be classified based on the following four basic types of single-phase and isolated full-bridge (FB) DC–DC converters: unidirectional isolated PSFB DC–DC converters, FB-LLC (inductor–inductor–capacitor) resonant converters, bidirectional PSFB DC–DC converters, and FB-CLLC (capacitor–inductor–inductor–capacitor) resonant converters.

2.1. Classification of Isolated DC–DC Converters Using SiC Devices

Figure 1a,b show an I-SiC-HFT which is used in unidirectional PSFB DC–DC converter and FB-LLC resonant converter. Each converter consists of four SiC MOSFETs connected to the primary winding of an HF transformer and four SiC Schottky diodes connected to the secondary winding of the HF transformer. However, the additional resonant capacitor, C_r , is not integrated within the HF transformer and SiC devices of the FB-LLC resonant converter. The leakage inductance can be used as the series inductance L_s for the PSFB DC–DC converter and as the resonant inductance L_r for the FB-LLC resonant converter. Therefore, the resonant capacitor is the only external component for the FB-LLC resonant converter.

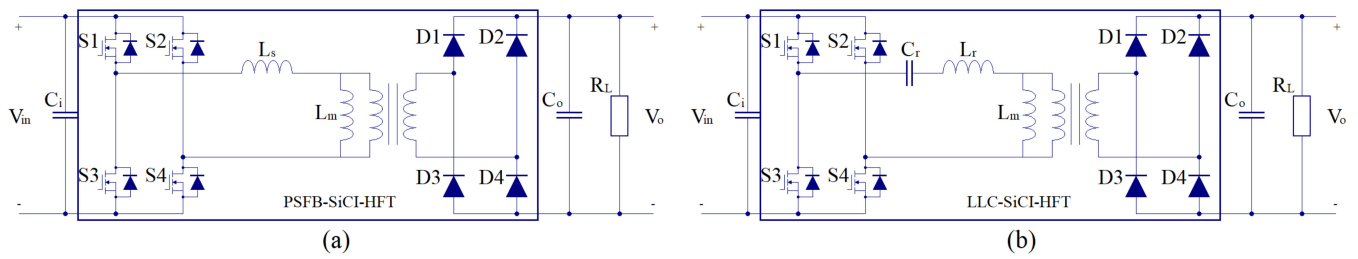


Figure 1. Unidirectional isolated DC–DC converters: (a) PSFB converter; (b) FB–LLC resonant converter.

Figure 2a,b present a bidirectional PSFB DC–DC converter and a bidirectional FB–CLLC resonant converter, where four SiC MOSFETs are connected to both the primary and secondary sides of an HF transformer to form a symmetrical structure in each type transformer. In these integrated structures, the leakage inductance of the HF transformer can be used as the series inductance for the bidirectional PSFB DC–DC converter and as the resonant inductance for the bidirectional FB–CLLC resonant converter. Thus, two resonant capacitors used for the CLLC resonant tank will be treated as external components in an I–SiC–HFT.

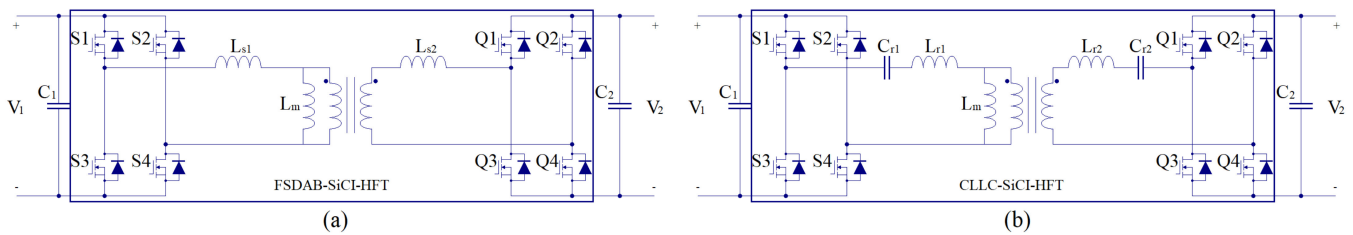


Figure 2. Bidirectional isolated DC–DC converters: (a) PSFB converter; (b) FB–CLLC resonant converter.

2.2. Phase-Shift Full-Bridge and Full-Bridge LLC DC–DC Converters

Isolated PSFB converters and FB–LLC resonant converters are normally used as buck–boost converters for DC power supply and provide unidirectional DC power flow with step-up or step-down HF transformers.

A. Phase-Shift Full-Bridge Converters

The PSFB DC–DC topology is carefully considered when designing for HP applications because of its advantages, which are reducing the voltage and current stress as well as having low ripple currents at the output filter and a low volt-ampere (VA) rating of the HF transformer.

The use of SiC–MOSFETs for a PSFB DC–DC converter allows both bridges to operate with synchronous rectification mode. Compared to pulse width modulation (PWM) which operates hard switching in all of the ranges of power transfer, the phase-shift control proposed in [16] can enable the PSFB DC–DC converter to achieve zero-voltage switching (ZVS) in a wide range of load conditions.

Snubber capacitors are connected in parallel with MOSFETs across the collector and the emitter to reduce switching loss and overvoltage. Snubbers particularly reduce turn-off overvoltage across the collector to the emitter of the MOSFETs so that ZVS can be achieved [4,17,18].

The total loss of a PSFB DC–DC converter comprises five loss components, including iron power loss (P_{iron}), switching power loss (P_{sw}), conduction loss (P_{cond}), copper loss (P_{copp}), and unknown power loss (P_{ukn}), as given by [19]:

$$P_{loss} = P_{iron} + P_{sw} + P_{cond} + P_{copp} + P_{ukn} \quad (1)$$

The unknown power loss may include the loss of the laminated DC-bus bars, temperature-dependent loss of SiC devices, AC winding loss due to skin and proxim-

ity effects, and power dissipated by the equivalent series and parallel resistances in the DC capacitors [19]. The conduction loss can be calculated as [17]:

$$P_{cond} = 2 * |i_1| * V_{CE(SAT)} + 2 I_2^2 * R_{DS}, \quad (2)$$

where R_{DS} is the sum of on-state and lead resistances of a MOSFET; $V_{CE(SAT)}$ is the collector to emitter saturated voltage; $|i_1|$ is the absolute average value of the primary current, and I_2 is the RMS value of the secondary current. The copper loss can be estimated by [17]:

$$P_{copp} = I_1^2 \cdot (R_{trans(HV)} + R_{ind(HV)}) + I_2^2 \cdot (R_{trans(LV)} + R_{ind(LV)}), \quad (3)$$

where I_1 is the RMS value of the primary current; R_{trans} and R_{ind} are the transformer winding resistance and the auxiliary inductor internal resistance respectively. The switching loss can be estimated by [19]:

$$P_{sw} = \frac{T_f^2}{48C} \cdot I_{sw}^2, \quad (4)$$

where I_{sw} is the switching current; $C = C_S + C_{ds}$ is the total capacitance calculated by snubber capacitance C_S and parasitic drain-to-source capacitance C_{ds} , and T_f is the falling time.

According to the analysis of a PSFB DC–DC converter presented in [18], the conduction loss and copper loss are independent of the iron loss. While changing the phase shift from 0° to 26° , the peak value of the magnetic flux in the transformer slightly decreases, which subsequently reduces the iron loss.

In [19], the total power-loss breakdown at the 750 V, 20 kHz and 100 kW under two snubber capacitance values of $C_S = 4.5$ nF and 9 nF, two switching power-loss calculations are $P_{sw} \propto I_{sw}^2$ and $P_{sw} \propto I_{sw}$. Under all different conditions, the conduction loss and switching loss have the highest proportions, while the switching loss slightly reduces by increasing the size of C_S .

B. Full-Bridge LLC Resonant Converters

To mitigate the losses during switching in the discontinuous conduction mode (DCM) and the harmonic losses of the square wave, the LLC resonant tank, also known as the LLC resonant network, becomes an effective topology [20,21]. An LLC resonant DC–DC converter can also achieve ZVS on both the primary and secondary sides of the transformer [22–24]. Hence, it is suitable for application in HF and HP devices, such as SiC semiconductor devices. It has many advantages over other conventional resonant converters, which include high efficiency, high power density, and low noise. It is also more reliable during high-frequency operation. Unlike conventional pulse width modulation (PWM) schemes, where the output can be changed with the duty cycle at a fixed switching frequency, LLC resonant converters work with pulse frequency modulation (PFM); they run at a constant duty cycle and frequency must be varied to achieve the desired output. Therefore, the regulation of LLC resonant converters can be obtained through frequency modulation. The output DC voltage in an LLC resonant converter contains low harmonics, and thus the overall efficiency of the system is much higher.

In an LLC resonant tank, the peak resonant frequency, f_{pr} , floats between the pole frequency, f_p , and the series resonant frequency, f_0 , i.e., $f_p \leq f_{pr} \leq f_0$, of the resonant tank as a function of load [25]. The pole frequency f_p and the series resonant frequency f_0 of an LLC resonant tank are defined by (5) and (6), respectively, in terms of the magnetising inductance L_m of the HF transformer, resonant inductance L_r , and resonant capacitance C_r [21,25]. The best operating point of the LLC resonant tank with the highest efficiency exists in the vicinity of the series resonant frequency, f_0 , where the benefits of the LLC resonant converter are maximised [21,25]. Thus, the switching frequency, f_s , of the LLC resonant converter should be equal to or slightly below the series resonant frequency, f_0 . Furthermore, the lifetime of the resonant capacitor is longer for a lower value of L_r and a higher value of C_r [21]. Therefore, the resonant inductance L_r should be minimized, and

the resonant capacitance C_r should be maximised to extend the lifetime of the resonant capacitor as much as possible [21]. The possible minimum value of L_r is restricted by the leakage inductance of the HF transformer. Consequently, the leakage inductance of the HF transformer should be used as the resonant inductance L_r , and no external inductor should be added to the tank circuit. To operate in the DCM, the LLC converter resonant components also need to satisfy the constraints described by (7) and (8) [21].

$$f_p = \frac{1}{2\pi\sqrt{(L_r + L_m)C_r}} \quad (5)$$

$$f_0 = \frac{1}{2\pi\sqrt{L_r C_r}} \quad (6)$$

$$\gamma = \frac{\omega_0}{2f_s} > \pi \quad (7)$$

where γ is the angular length of the one-half switching period, and $\omega_0 = 2\pi f_0$ is the resonant angular frequency.

$$I_o < 8f_s C_r V_o \quad (8)$$

where I_o is the load current, and V_o is the output voltage.

Under light loading conditions, the peak of the characteristic moves close to f_p , and under heavy loading conditions, the peak moves close to f_0 . Under different loading conditions, a DC characteristic shown in Figure 3 is partitioned into different regions. Region 1 is the operating region of the proposed converter in which ZVS condition is naturally achieved. Region 2 is categorized where the load condition between f_0 and f_p decides the converter operation under ZVS and zero-current switching (ZCS) conditions. This is called a multi-resonant converter region. The LLC resonant converter is fully operated in ZCS mode in the overloaded region marked as Region 3. SiC MOSFETs are generally preferred for designing the LLC resonant converter, which allows HF operation and ensures lower switching loss. This can be achieved by choosing proper values of L_m , L_r and C_r .

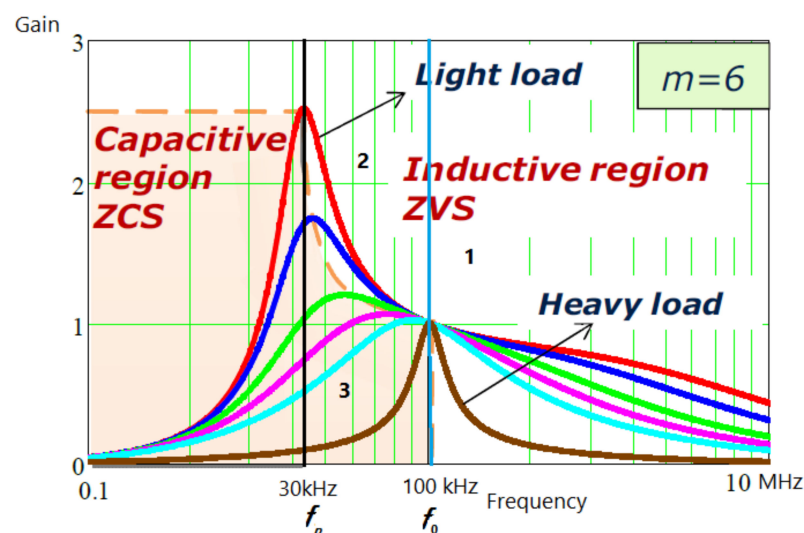


Figure 3. The characteristics of the LLC resonant converter [26].

The design parameters are calculated using the gain equation as described in the references [27–29] and considering harmonics approximation. The resonant tank gain can

be derived by analysing the equivalent resonant circuit shown in Figure 4, and the resonant tank gain G_c is the magnitude of its transfer function as in (9) [22].

$$G_c = \left| \frac{L_1 f_1^2}{[f_1^2(L_1 + 1) - 1] + j[(f_1^2 - 1)L_1 Q f_1]} \right| \tag{9}$$

$$f_1 = \frac{f_s}{f_0} \tag{10}$$

$$L_1 = \frac{L_m}{L_r}, L_m = \frac{t_{dead}}{16C_s f_0} \tag{11}$$

$$Q = \frac{Z_r}{R_{ac}} = \sqrt{\frac{L_r}{C_r} / n^2 R_o}, C_r = \frac{2\pi f_0}{Z_r} \tag{12}$$

where f_1 is the normalized frequency; L_1 is the inductance ratio; Q is the quality factor; n is the transformer turns ratio; t_{dead} is the dead time of the driving circuit; C_s is the output capacitance of the switches, and R_o is the effective load resistance.

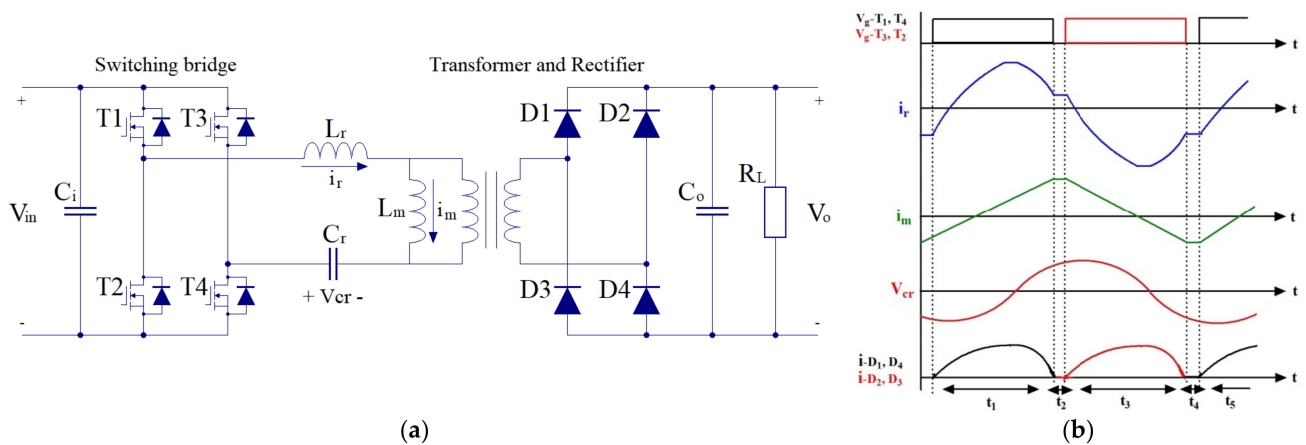


Figure 4. FB-LLC resonant converter with FB rectifier: (a) Two inductors and one capacitor forming a resonant circuit; (b) Output waveforms of the FB-LLC resonant converter [22].

The switching bridge generates a square waveform to excite the LLC resonant tank, which will output a resonant sinusoidal current that gets scaled and rectified by the transformer and rectifier circuit. The output capacitor filters the rectified AC current and outputs a DC voltage. Figure 4 illustrates an overview of the FB-LLC resonant converter operation and waveforms in different time intervals.

All primary side SiC MOSFETs turn on resonantly with ZVS, resulting in full recycling of the energy contained in the SiC MOSFETs’ parasitic output capacitance. Furthermore, all secondary side switches turn off resonantly with ZCS to minimize switching losses normally associated with hard switching. Resonant operation of all switching devices in the LLC resonant converter results in minimized dynamic loss and thus increased overall efficiency, particularly at higher operating frequencies in the hundreds of kilohertz to megahertz range.

2.3. Bidirectional Phase-Shift Full-Bridge and Full-Bridge CLLC DC–DC Converters

A. Bidirectional Phase-Shift Full-Bridge Converters

A bidirectional PSFB DC–DC converter is composed of two active bridges with an HF transformer controlled by phase-shift control. The PSFB DC–DC converter can operate either in buck mode or boost mode, depending upon the requirement of the application [30].

The PS modulation technique is simple to design and commonly used for HP applications. In steady-state operation, changing the sign of phase shift allows changing the

power flow direction in order to achieve bidirectional operation of the converter [31,32], while the duty cycle can be selected to be fixed or variable depending upon the control design [33,34].

Typical phase-shift modulation schemes for bi-directional PSFB DC–DC converters are single phase-shift (SPS), extended phase-shift (EPS), dual phase-shift (DPS), and triple phase-shift (TPS) [1]. Figure 5 demonstrates the key waveforms of SPS, EPS, and DPS modulation schemes.

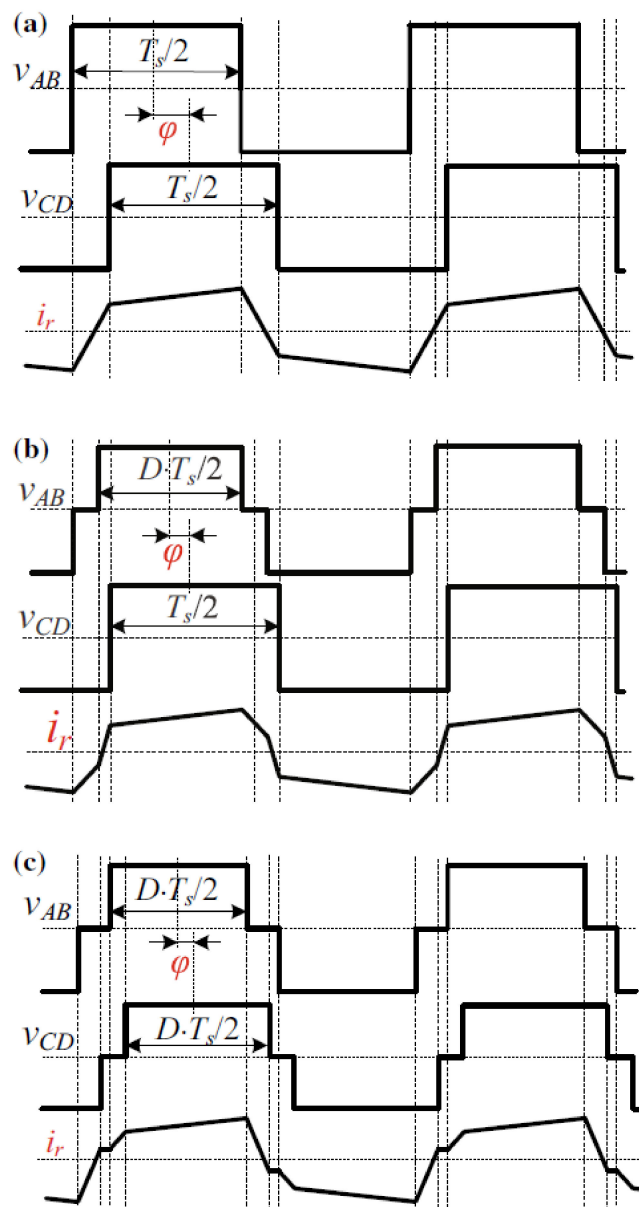


Figure 5. Waveforms of typical PS modulation schemes: (a) SPS; (b) EPS; (c) DPS [1].

SPS control is the most conventional phase-shift modulation due to its simple design and having one degree of freedom [35,36]. This type of phase shift is commonly used in different applications because of its advantages: less inertia, high dynamics, and soft-switching control [37]. High efficiency can be achieved if the input and output voltages are matched to the transformer turns ratio, and to allow transferring maximum power, the

phase angle should be limited between $-\frac{\pi}{2}$ and $\frac{\pi}{2}$ [36]. The transmission power using SPS can be calculated by [37]:

$$P = \frac{nV_iV_o}{2f_sL} \cdot D(1 - D) \quad (13)$$

where n is the transformer turns ratio; V_i is the input voltage; V_o is the output voltage; f_s is the switching frequency; L is the equivalent inductance of transformer leakage inductance and auxiliary inductance, and D is the phase shift ratio.

The EPS control method is proposed to reduce the circulating current and backflow power [38,39]. In the EPS method, the full bridge at the primary side of the HF transformer generates a two-level square waveform, and the secondary side bridge generates a three-level square waveform. This operation is performed by adjusting the duty cycle, which can be calculated by the loss breakdown analysis presented in [40,41]. The transmission power using EPS can be calculated by [39]:

$$P = \frac{nV_iV_o}{2f_sL} \cdot \left[\frac{1}{2}D_1(1 - D_1 - 2D_2) + D_2(1 - D_2) \right] \quad (14)$$

The DPS control method improves efficiency [42,43]. In DPS, both full bridges at the primary and secondary sides generate three-level waveforms with the same duty cycle. This phase shift technique has two degrees of freedom, which are the inner phase shift angle and the outer phase shift angle [44]. As a result, the circulating current and current stress can be reduced [1,44]. The transmission power using DPS can be calculated by [44]:

$$P = \frac{nV_iV_o}{2f_sL} \cdot [D_2(1 - D_2) + 0.5D_1(2D_2 - D_1 - 1)] \text{ when } D_2 > D_1 \quad (15)$$

$$P = \frac{nV_iV_o}{2f_sL} \cdot (1 - D_1) \cdot (D_2 - 0.5D_1) \text{ when } D_2 < D_1 \quad (16)$$

Using a DPS method in [45], the reactive power can be eliminated from the PSFB DC–DC converter, and the system power capacity is increased by 33% compared with the conventional SPS control method.

TPS is proposed to improve the overall performance of the converter, especially when operating at low power, and to increase the range of ZVS and reduce the total power loss thanks to its three control variables: duty cycle of the primary bridge, duty cycle of the secondary bridge, and the phase shift between them [46]. While this method exhibits the better performance of the PSFB DC–DC converter, the higher number of the required switching modes in the TPS method increases the complexity of implementation. For instance, in [47], four TPS switching modes are studied to extend ZVS operation and efficiency. In [48], six switching modes are investigated using detailed analytical investigation. In [49], twelve TPS switching modes are identified to reduce the conduction loss under the ZVS range. The transmission power using TPS can be calculated by [50]:

$$P = \frac{nV_iV_o}{2f_sL} \cdot \left[\frac{1}{2}(D_2 - D_1 - D_3) \cdot (D_2 + D_3 - 1) \right] \quad (17)$$

B. Bidirectional Full-Bridge CLLC Resonant Converters

The bidirectional FB-CLLC resonant converter is widely used in battery charging systems (including EV on-board chargers and V2G EV charging systems) and AC and DC microgrid energy storage in renewable energy systems because of its advantages of high-power density and its capacity for bidirectional power transfer [51–53]. The bidirectional FB-CLLC resonant converter with its symmetric resonant tank, soft switching characteristics, and ability to switch at higher frequencies is commonly used for the above applications [54–57].

The bidirectional FB-CLLC resonant converter consists of two FB circuits and a resonant network. Figure 6a shows the bidirectional FB-CLLC resonant converter which consists of two leakage inductances (L_{r1} and L_{r2}) and two capacitors (C_{r1} and C_{r2}), forming a sym-

metric resonant circuit [51]. The proposed I-SiC-HFT includes two leakage inductances (L_{r1} and L_{r2}), the transformer magnetizing inductance (L_m), and two FB SiC MOSFETs. Two capacitors (C_{r1} and C_{r2}) will be external components. Switches S_{i1} – S_{i4} and S_{o1} – S_{o4} form two FB circuits, respectively, L_{r1} , L_{r2} , C_{r1} , C_{r2} , and L_m form two resonant networks in different states, and HF transformer T_r acts as an electrical isolator. The FB-CLLC resonant converter operates in the forward direction by applying complementary drive signals to S_{i1} and S_{i2} to achieve inversion when the body diodes of S_{o1} and S_{o2} are used to achieve rectification. In reverse operation, the primary and secondary switches swap operating states for reverse power transfer. In this topology, the primary and secondary switches can achieve soft switching, effectively improving the conversion efficiency of the converter.

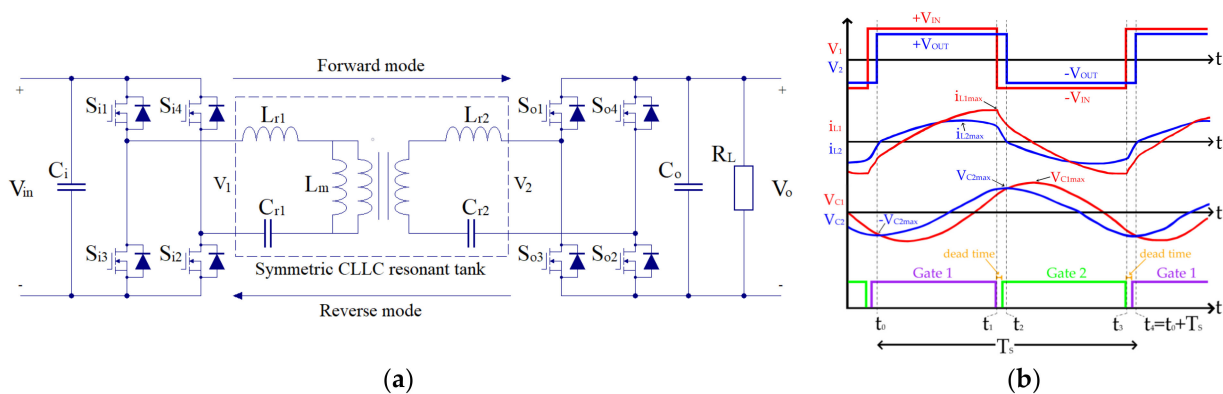


Figure 6. Typical bidirectional FB-CLLC resonant converter: (a) Operation of forward and reverse modes; (b) Waveforms of the resonant frequency in the forward mode.

Figure 6a indicates the voltage polarities and current directions for both forward and reverse mode during the energy conversion. Since the FB-CLLC resonant converter has a symmetric structure of the circuit, the analysis of the converter is the same for both cases. The analysis of the converter in the forward (forward power flow direction) mode can be performed in the same manner by exchanging the notations of voltage V_{in} and V_{out} , and leakage inductances (L_{r1} and L_{r2}) and capacitors (C_{r1} and C_{r2}) in the CLLC resonant tank. The primary active full bridge is composed of four SiC MOSFETs. The switching network of the secondary side is also formed in a similar manner as the synchronous rectifier. The resonant tank comprised capacitors C_{r1} and C_{r2} , the transformer magnetizing inductance L_m , and the primary and secondary leakage inductances L_{r1} and L_{r2} . Depending on the desired power flow direction, the bridge of the primary side of the HF transformer acts as an inverter, and the bridge of the HF transformer's secondary side acts as a synchronous rectifier [51–53].

Typical waveforms of the FB-CLLC converter are shown in Figure 6b, assuming that the converter operates in the continuous conduction mode and the secondary-side full-bridge acts as a diode rectifier, where the gate signals of transistors S_{o1} to S_{o4} are applied at the i_{i2} zero crossing, i.e., t_2 and t_4 . Depending on the switching state and the secondary-side current, the CLLC resonant converter operates in four possible operation modes during subinterval 1 ($t_0 \leq t < t_1$), subinterval 2 ($t_1 \leq t < t_2$), subinterval 3 ($t_2 \leq t < t_3$), and subinterval 4 ($t_3 \leq t < t_4$) in a complete switching period [52].

During both the forward power flow mode and reverse power flow mode, the operation boundary follows (5) to (12) but needs to use the corresponding values for the input side of the power. The ZVS operation of the primary power SiC MOSFETs and the soft commutation of the output rectifiers are significant factors for the efficiency-optimal design of the bidirectional FB-CLLC resonant converter. The primary current should discharge the output capacitance C_s of four primary switches during the dead time for their ZVS

turn-on. The ZVS condition of the switches depends on the magnetizing inductance L_m and the dead-time duration t_{dead} as [51]:

$$t_{dead} \geq 16C_s f_{s,max} L_m \quad (18)$$

An operating (switching) frequency that is lower than or equal to the resonant frequency can guarantee the soft commutation of the output rectifiers. Therefore, the magnetizing inductance L_m of HF transformer is limited by the maximum switching frequency $f_{s,max}$ as in (11).

2.4. Comparison between Phase-Shift Full-Bridge/Bidirectional Phase-Shift Full-Bridge Converters and Full-Bridge LLC/Bidirectional Full-Bridge CLLC Resonant Converters

FB-LLC resonant converters can be used for many different HP DC power supplies, and they are the most efficient solution for point-of-load converter applications. They also have high efficiency and less electromagnetic interference (EMI) noise. However, for easier design and more flexible and robust systems, PSFB DC–DC converters are a better option. The main difference between a FB-LLC resonant converter and a PSFB DC–DC converter is the method of operation as well as the stress in the components. However, bidirectional FB-CLLC resonant converters and bidirectional PSFB DC–DC converters are mainly used for V2G, battery charging in microgrids, and renewable energy systems. Table 1 indicates the advantages and disadvantages of the HP I-SiC-HFT module with different DC–DC converter topologies.

Table 1. Advantages and disadvantages of the HP I-SiC-HFT with different DC–DC converter topologies.

Power Electronic Topology	Unidirectional FB-LLC	Unidirectional PSFB	Bidirectional FB-CLLC	Bidirectional PSFB
Suitability of I-SiC-HFT	High	High	High	High
Magnetic component design	Easy	Easy	Easy	Easy
Switching loss	Low	Medium	Low	Medium
EMI problem	Low	Low	Low	Low
Power loss	Low	Low	Low	Low
Thermal problem	Less	Less	Less	Less
Power efficiency	>98%	>98%	>98%	>98%
High-power applications	Yes	Yes	Yes	Yes

In addition, the design consideration of the magnetizing inductance L_m and leakage inductance L_r must be carefully considered as there is no commercially available HF transformer for the application. Therefore, after L_m and L_r are calculated from the FB-LLC/CLLC circuit design, the HF transformer design will be another challenging task. The detailed HF transformer design and the L_m and L_r optimised for PSFB converter and FB-LLC resonant converter, and bidirectional PSFB converter and FB-CLLC resonant converter will be discussed in later sections.

3. Architecture of Integrated SiC-Device and High-Frequency Transformer

3.1. Compact Structure of Integrated SiC-Device and High-Frequency Transformer

Generally, there are four different types of single-phase core constructions suitable for HF transformers, which are core type, shell type, coaxial winding type, and matrix type [58–60], as illustrated in Figure 7. However, coaxial winding transformers are not well suited for HP applications because of their limited current carrying capability in their tubular structure resulting in limited power capability [58,59]. In the core-type transformer construction, the primary and secondary windings, or half of both windings, are wound around the two limbs of the core ring, allowing the transformer height to be reduced [58,61]. However, since less surface is exposed to air as compared to the

shell-type transformer construction, the coils have less mechanical protection as well as overall poor thermal dissipation [58,59,62]. In the shell-type transformer construction, both the primary and secondary windings are wound around the middle limb, leading to better mechanical protection for the coils and more effective cooling. In the matrix-type transformer construction, multiple pairs of magnetic cores are commonly used to form a radial shape, where the primary HV winding is wound around the central limbs, and each separated secondary low-voltage (LV) winding is wound around the outer limb of each core to establish parallel outputs. Hence, it has the merits of HP handling ability, height reduction, good thermal dissipation, and lowering HV winding turns [58,59,61]. Nevertheless, the use of multiple separated magnetic cores brings about the use of more semiconductor devices and an increase in mass and volume, and the separated primary and secondary windings result in difficulties in controlling the total leakage inductance [58,59].

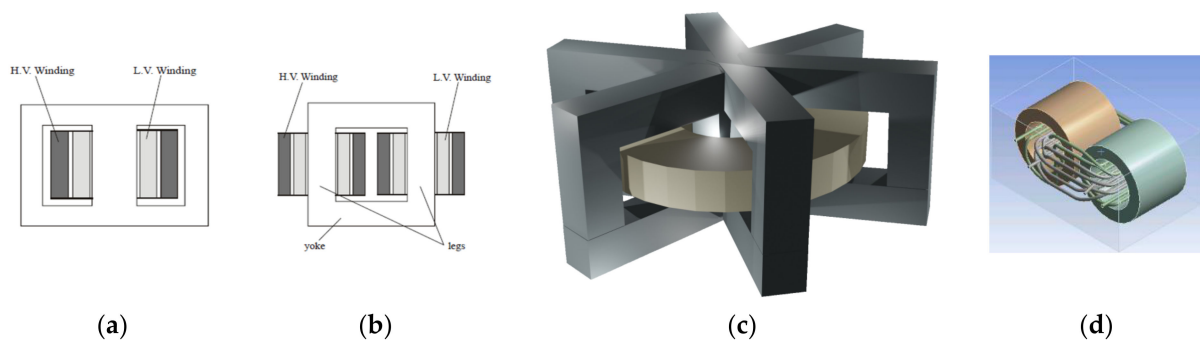


Figure 7. Various HF transformers and their magnetic core structures. (a) Shell type (b) Core type (c) Matrix type (d) Coaxial type.

Figure 8 shows several HF transformers used for DC–DC converters, where shell-type transformers and coaxial transformers are normally used for LLC resonant converters and PSFB converters, respectively [63,64]. However, planar transformers can be used for both LLC resonant converters and PSFB converters [65].

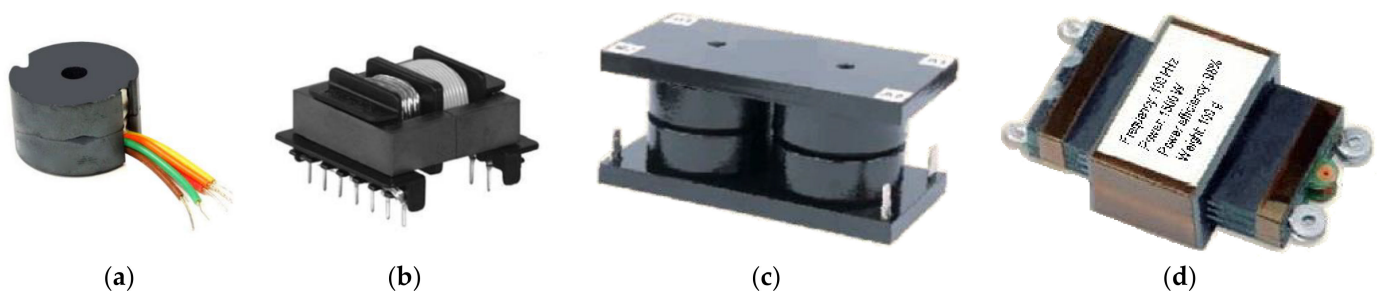


Figure 8. HF transformers used for LLC resonant converter and PSFB converter and their magnetic core structures. (a) Pot-core transformer (b) Shell-type transformer (c) Coaxial transformer (d) Planar transformer.

In existing HP isolated DC–DC power converters, DC–AC and AC–DC conversion circuits cannot be integrated into the HF transformers because there is no room for SiC semiconductor devices to be installed inside an HF transformer based on the aforementioned transformer core geometries. However, SiC semiconductor devices can be integrated within the proposed transformer construction by installing them inside the transformer, provided the inner hollow part of the transformer is big enough.

The proposed HF transformer construction, which is somewhat similar to the matrix type, is composed of multiple discrete pairs of U-shaped magnetic cores in a radial (toroidal/annular) arrangement with both the primary and secondary windings wound around the inner central limbs. In addition, the space needed for the SiC semiconductor devices is considered and reserved in this proposed transformer structure. Figure 9 illus-

trates the schematic of the I-SiC-HFT. The proposed HF transformer structure can construct HP transformers of any power level with integrated SiC devices. Therefore, the proposed I-SiC-HFT has the advantages of mass and volume reduction for isolated DC–DC power converters, efficient cooling, good coil mechanical protection, winding turns reduction, and easy adjustment in leakage inductance using different winding patterns; its only handicap is not being well suited for low-power applications.

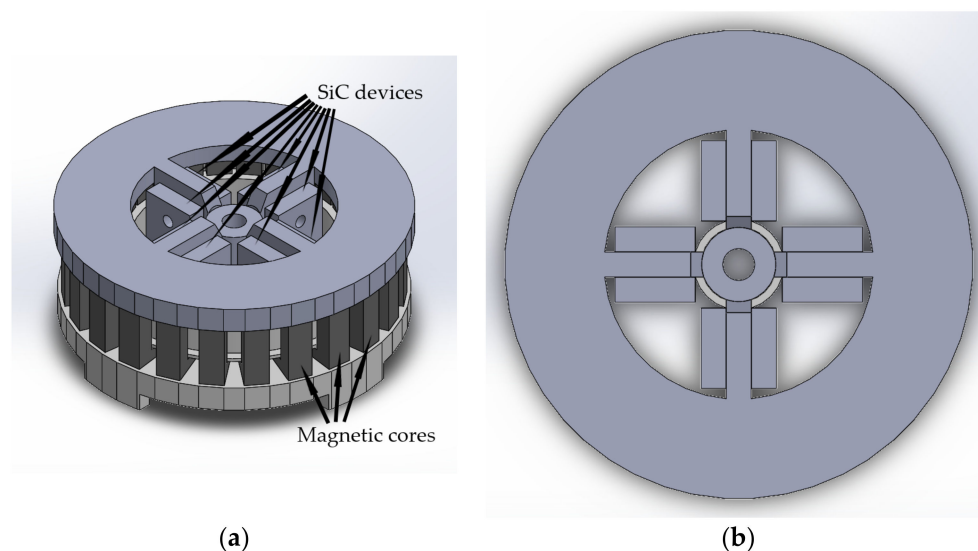


Figure 9. Schematic of integrated SiC-device and HF transformer. (a) Isometric view (b) Top view.

Compared with other currently existing HF transformer structures as shown above, the proposed HF transformer can achieve the same power density as a pot core-based HF transformer. Obviously, an HF toroidal transformer has a larger central area or hole than the pot core transformer, but it cannot be used because of the EMI problem and strong magnetic leakage flux distributed in the central area. For other, ordinary HF transformers, SiC devices need to be installed separately with the heatsink outside the transformers, and hence the total size of the isolated DC–DC converter will be increased. In contrast to the proposed HF transformer with integration of SiC devices, the power density for a totally isolated DC–DC converter or DC transformer, which includes SiC semiconductor devices, is relatively high. Compared with toroidal core-based HF transformer structure used for isolated DC–DC converters, further volume/size reduction can be achieved for HP applications by using the proposed HF transformer with SiC MOSFET modules. Comparison of the proposed HF transformer with other traditional HF transformers including other aspects are presented in Table 2.

3.2. Design Considerations of SiC-Device-Integrated High-Frequency Transformer

3.2.1. Winding Structures

Transformer AC winding losses are caused by the skin and proximity effects [66]. These effects are frequency dependent, increasing as frequency increases, and the losses caused by these effects also increase and become significant as frequency increases. However, the losses due to these effects can be reduced to a minimum by selecting the right-size Litz wire or flat (foil) wire and by reducing the transformer winding layers [67]. Generally, there are three different winding structures: separate winding structure, concentric winding structure, and interleaved winding structure. Among these types of winding structures, the separate winding structure causes the highest leakage inductance of an HF transformer as it has the largest fraction of magnetic flux that is not coupled by the primary and secondary windings [68]. The concentric winding structure produces higher leakage inductance as compared to the interleaved winding structure. The leakage inductance, parasitic capacitance, and winding AC resistance can be controlled by adjusting the

separation between the primary and secondary windings in the separate and concentric winding structures, and by changing the alternating patterns in the interleaved winding structure [66,69–76]. Figure 10 shows the magnetomotive force distributions for three different winding arrangements.

Table 2. Comparison of the proposed HF transformer with other HF transformers.

Transformer Type/Structure	Advantages	Disadvantages
Core type	Easy to repair Well-suited for HP applications	Poor cooling Less mechanical protection to coils Difficult to tune leakage inductance
Shell type	Effective cooling Better mechanical protection to coils Well-suited for HP applications Better mechanical protection to coils	Not easy to repair
Pot core transformer	Low EMI problem High power density	Low power ratings
Toroidal transformer	Easy to construct and repair	Less mechanical protection to coils High EMI problem
Coaxial transformer	Suitable for HF applications Small in size and weight	Low power ratings
Planar transformer	Low to medium power applications	High interwinding capacitance
Matrix transformer	Advantages of both core and shell-type transformers	Higher weight and volume Difficult to tune leakage inductance
Proposed transformer	Advantages of both core-type, shell-type, and pot core transformers Integration with SiC devices feasible	Not well-suited for very low-power applications—higher weight and volume

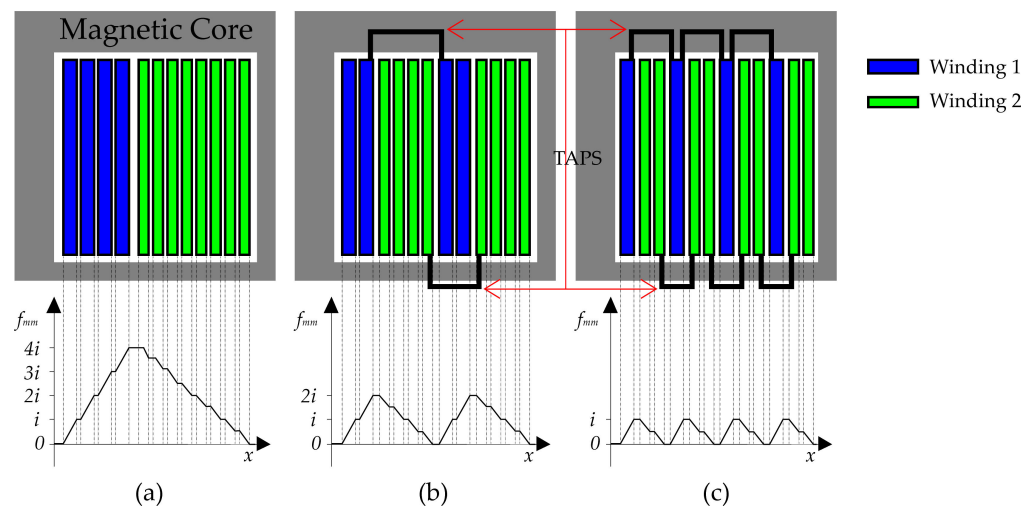


Figure 10. Magnetomotive force distributions for different winding configurations: (a) non-interleaved; (b) partially interleaved; (c) fully interleaved.

3.2.2. Electromagnetic Compatibility

In EMI, there are four coupling mechanisms: conductive, inductive (magnetic), capacitive (electric), and radiative (electromagnetic) [77]. For an I-SiC-HFT, the HF transformer and SiC devices can be both the sources and the victims of EMI because they all conduct electric and magnetic waves. The circulation of magnetic flux in the HF transformer can barely be impacted by the air gaps between two neighbouring pairs of U cores, since the magnetic cores, where almost all the induced magnetic flux is confined, have considerably greater permeability than air. Thus, the leakage inductance in the air should be insignificant to produce unacceptable inductive EMI that can influence the normal and proper

operation of the SiC devices which are integrated within the HF transformer. In addition, the unwanted HF EMI produced by the integrated SiC devices due to fast switching speed and switching ringing can be suppressed to an acceptable level by soft-switching techniques [78–81].

3.2.3. Thermal Management and Cooling Methods

An HP I-SiC-HFT will generate a substantial amount of heat, so proper cooling is required. The thermal management of the I-SiC-HFT is more straightforward; since more surface area is exposed to air for heat extraction, it is less complex than the core-type and shell-type transformers. Heatsinks and forced cooling systems, such as an electric fan, can be used to extract the heat generated by the I-SiC-HFT. Since the discrete SiC devices or SiC modules are installed and attached against the inner walls of the HF transformer, U-type heatsinks can be placed at the back of the SiC devices, and a CPU cooling fan can be installed on the top of the heatsinks. Figure 11 shows an example of a cooling scheme for the I-SiC-HFT with SiC devices. For the HP application, as shown in Figure 12, L type heatsinks will be placed at the back of each SiC MOSFET module and centre arms of the HF transformer. In this case, a strong electric cooling fan will be installed on the top of the heatsinks for thermal management.

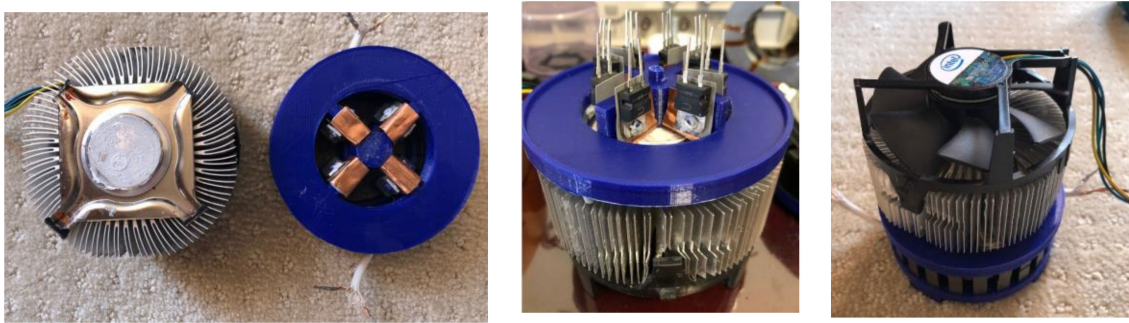


Figure 11. Cooling scheme of the integrated SiC devices and HF transformer.

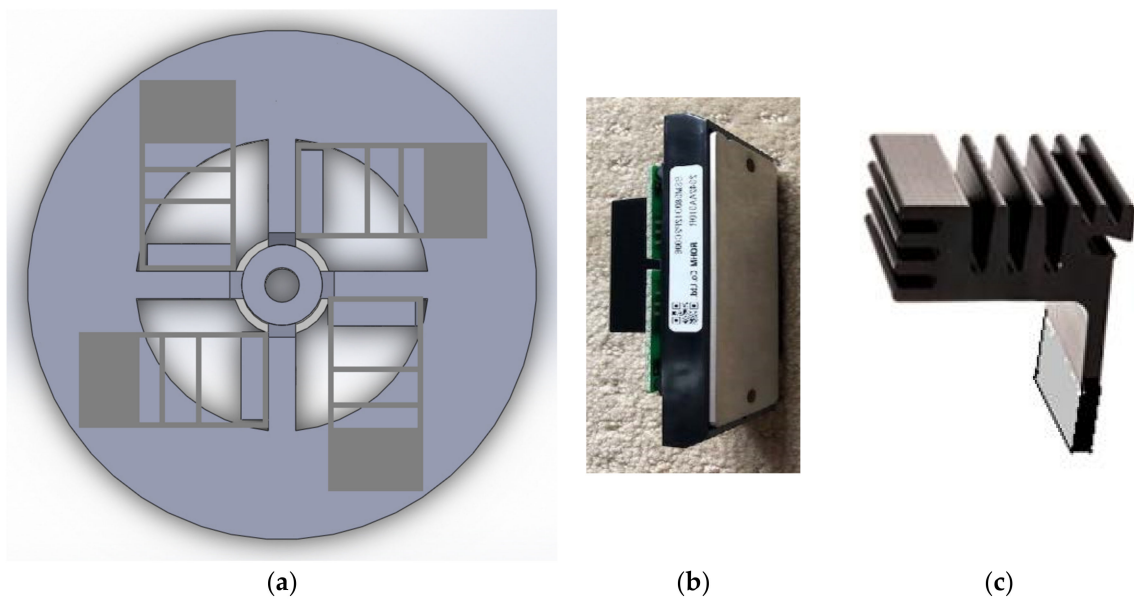


Figure 12. Cooling scheme of the integrated SiC-MOSFET module and HP HF transformer: (a) I-SiC-HFT; (b) SiC MOSFET module with gate drive; (c) L type heatsink attached to heatsink pad of SiC MOSFET module.

4. Design and Implementation of SiC-Device-Integrated High-Frequency Transformer

This section presents the design, implementation, simulation results, and experimental results of a small-scale laboratory prototype I-SiC-HFT. Since the prototype was designed and built as proof-of-concept, only a full-bridge rectifier was integrated within the HF transformer, and hard-switching technique was used because of the ease of implementation. If the prototype I-SiC-HFT works well even in the worst, most extreme case of hard switching conditions, then it will operate well in soft switching conditions.

4.1. Transformer Core Material and SiC Device Selection

The prototype I-SiC-HFT was designed based on a DC chopper modified from a Transphorm 3.0 kW inverter evaluation kit (TDINV3000W050-KIT), so the rated power and primary voltage of the prototype I-SiC-HFT were chosen to be 1.5 kW and 375 V respectively, which are safely below the specifications of the inverter. For the proof of concept, SiC Schottky diodes were chosen to be integrated within the prototype HF transformer.

Since the power rating of the transformer is 1.5 kW, the smallest U cores, U15/11/6, from TDK were chosen and used. If larger cores were used, then the shell-type or core-type structure would be adequate for the transformer because the U core of the next size up is much bigger than the chosen one. Otherwise, there would be a waste of material for the proposed structure using larger U cores. Since the U15/11/6 cores were made from Mn-Zn ferrite N27 with the maximum optimum operating frequency of only 150 kHz, the operating frequency of the prototype transformer was designed to be 100 kHz, well below the upper limit. The SiC Schottky diodes, S3D06065, from SMC Diode Solutions were chosen to be used for the prototype as their rated voltage and current meet the requirements. The prototype requirements shown in Table 3 are based on all the above-mentioned factors. Several properties of ferrite N27 and S3D06065 are listed in Tables 4 and 5 respectively.

Table 3. Design specifications for the prototype HF transformer.

Variable	Value
Power rating	1.5 kW
Rated primary voltage	375 Vrms
Rated primary current	4 A
Operating frequency	100 kHz
Maximum current density	$5 \times 106 \text{ A/m}^2$ (5 A/mm ²)
Window utilization factor	≤ 0.25
Type of transformer	Isolation transformer

Table 4. Several properties of ferrite N27.

Electromagnetic Property of N27	Value
Resistivity	3 $\Omega \cdot \text{m}$
Initial relative permeability	2000
Saturation flux density	0.41 T ¹
Core loss density	920 kW/m ³ ²
Operating frequency range	up to 150 kHz

¹ Typical value under conditions: 10 kHz and 100 °C; ² Typical value under conditions: 100 kHz, 0.2 T, and 100 °C.

Table 5. Some characteristics of SiC Schottky diode S3D06065.

Characteristics of S3D06065	Condition	Value
DC blocking voltage, Peak repetitive reverse voltage, Working peak reverse voltage	-	650 V
Average rectified forward current	$T_c = 157 \text{ }^\circ\text{C}$	6 A
Forward voltage drop	6A, pulse, $T_j = 175 \text{ }^\circ\text{C}$	1.9–2.4 V
Junction capacitance	$V_R = 0 \text{ V}$, $T_j = 25 \text{ }^\circ\text{C}$, $f = 1 \text{ MHz}$	382 pF
Power dissipation	$T_j = 110 \text{ }^\circ\text{C}$	45 W

4.2. Transformer Design Method for Phase-Shift Full-Bridge and Full-Bridge LLC Converters

The turns ratio of the prototype HF transformer needs to meet the input-to-output voltage ratio for the PSFB and FB-LLC soft switching techniques. The required turns ratios, n , for the HF transformer are calculated as in (19) and (20) for PSFB and FB-LLC converters, respectively.

$$n = \frac{N_p}{N_s} = \frac{(V_{in} - 2 \times V_{MOSFET_on}) \times D}{V_o + 2 \times V_{diode_on}} \quad (19)$$

$$n = \frac{N_p}{N_s} = \frac{V_{in} - 2 \times V_{MOSFET_on}}{V_o + 2 \times V_{diode_on}} \quad (20)$$

where N_p is the number of primary turns; N_s is the number of secondary turns; V_{in} is the input DC voltage; V_o is the output DC voltage; V_{MOSFET_on} is the gate-source turn-on voltage of the SiC MOSFET, and V_{diode_on} is the forward voltage drop of the SiC Schottky diode.

Based on all the aforementioned factors and specifications, the design results of the HF transformer are listed in Table 6.

Table 6. Design outcomes of the prototype HF transformer.

Transformer Parameter	Designed Value
Number of pairs of U cores	24
Maximum magnetic flux density	0.3 T
Number of strands for primary coil	7 strands
Number of strands for secondary coil	7 strands
Number of primary turns	5 turns
Number of secondary turns	6 turns
Turns ratio	1:1.2

4.3. Simulation and Experimental Results

4.3.1. 3D FEM Simulation Results

The 3D model of the prototype HF transformer was created in COMSOL, and the 3D simulation was performed based on the finite element method (FEM), which is the most effective and accurate numerical method for transformer modelling and simulation.

Figure 13 illustrates the 3D simulation model of the prototype HF transformer. In this model, the space for the transformer clips, bobbin, and SiC Schottky diodes are considered and reserved, and the primary and secondary windings are simplified by two separated homogenized multi-turn winding blocks with an air gap of 1 mm, which is the same as the partition in the real winding structure, to mitigate the redundant computational processes. Figure 14 exhibits the magnetic flux density distribution in the ferrite cores under the full-load condition at 100 kHz, and Figure 15 demonstrates the magnetic flux distribution in the entire model, including the free space in the air under the full-load condition at 100 kHz. Table 7 presents the simulation findings.

Table 7. COMSOL simulation results of the prototype HF transformer at the full-load condition and 100 kHz.

Transformer Parameter	Simulated Value
Maximum magnetic flux density	0.33604 T
Mutual inductance	281.51 μ H
Primary leakage inductance	5.7404 μ H
Secondary leakage inductance	8.2660 μ H
Voltage ratio	1.1955
Primary voltage	375.53 V
Secondary voltage	448.95 V
Primary current	3.9943 A
Secondary current	3.3255 A
Primary power	1499.979 W
Secondary power	1492.983 W
Transformer efficiency	99.53%

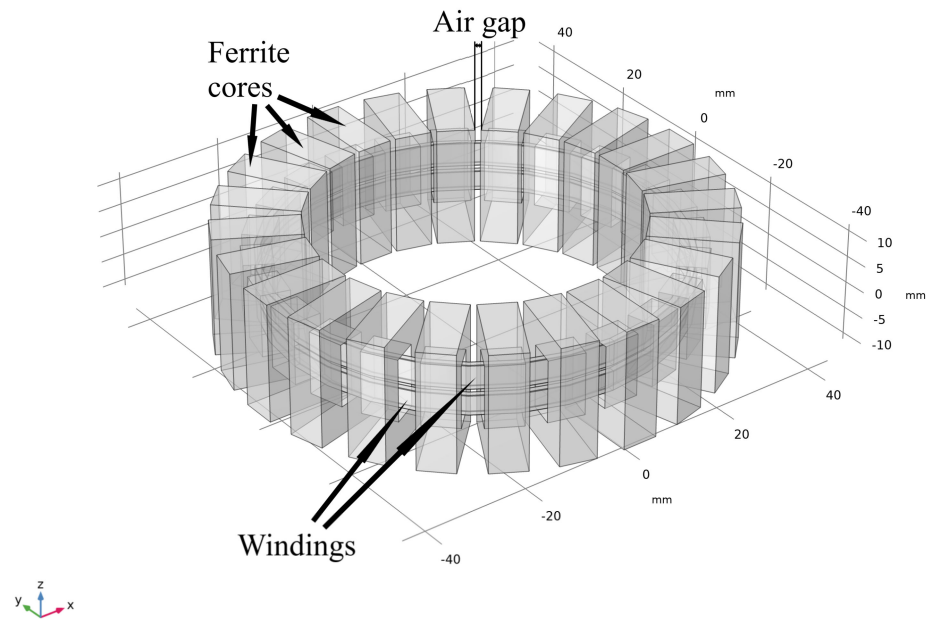


Figure 13. COMSOL simulation model of the prototype HF transformer.

freq(1)=100 kHz

Volume: Magnetic flux density norm (T) Arrow Volume: Magnetic flux density

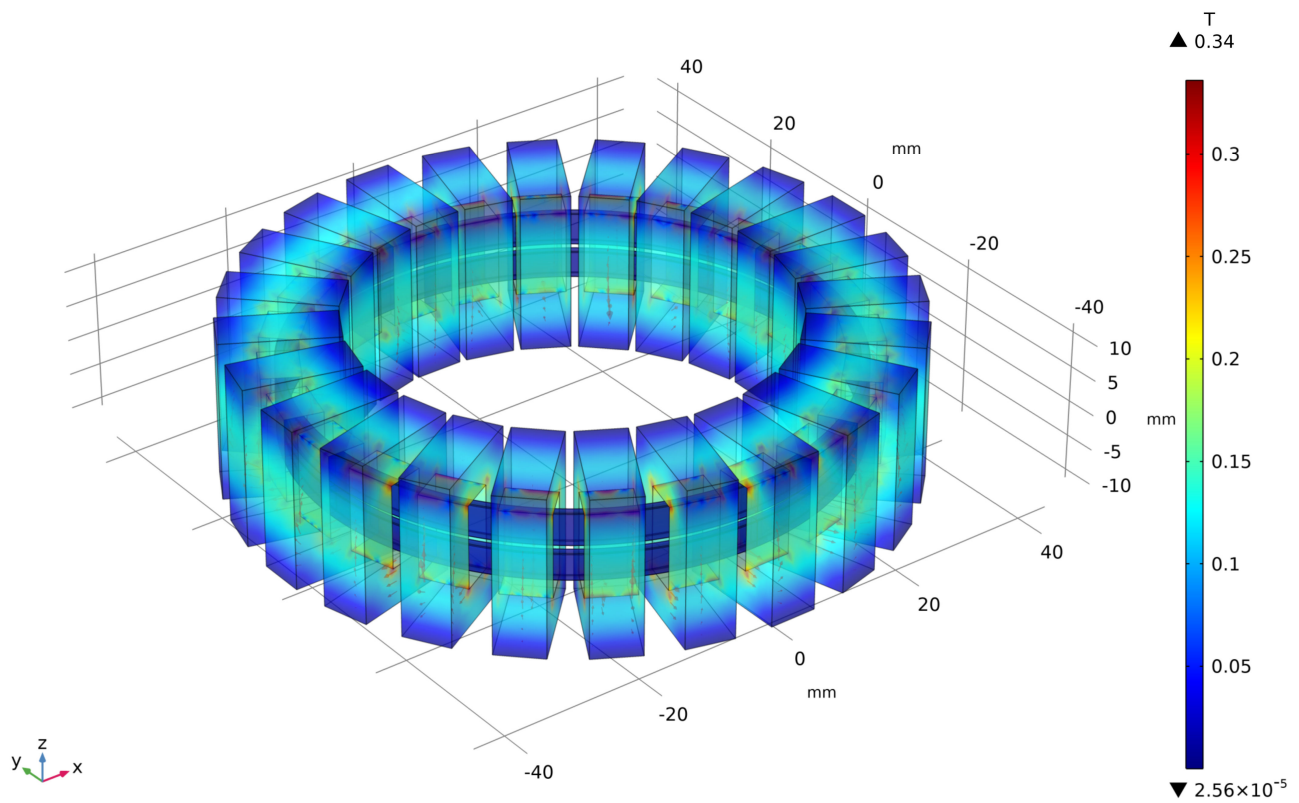


Figure 14. Magnetic flux density distribution in the ferrite cores at full-load condition and 100 kHz (air domain not shown).

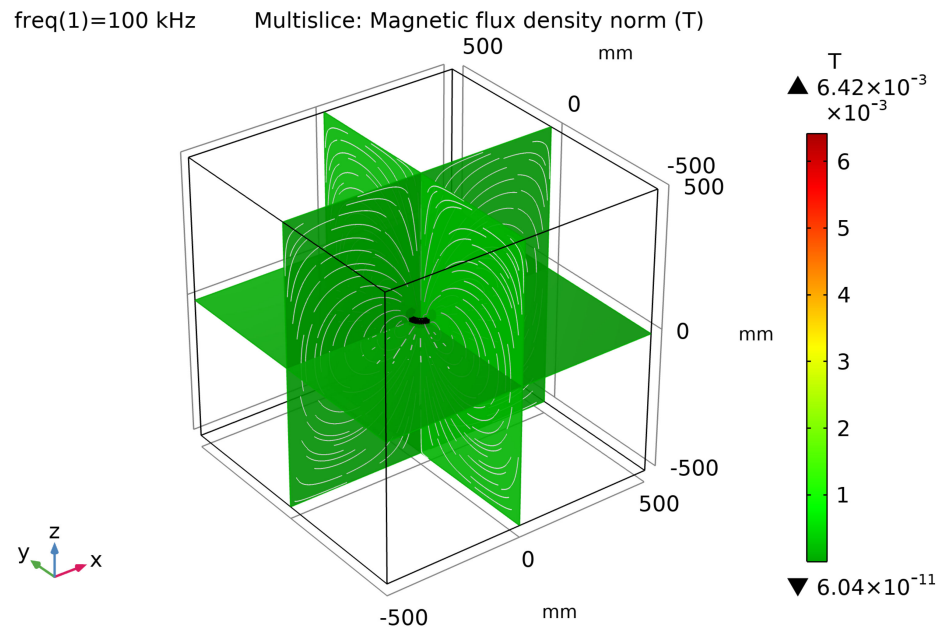


Figure 15. Leakage magnetic flux distribution in the whole model, including the air domain at the full-load condition and 100 kHz.

The simulated maximum magnetic flux density is 0.03604 T higher than the designed value, occurring only at and near the sharp inner corners of the ferrite cores, where the magnetic paths are uneven. Hence, the simulated and designed maximum magnetic flux densities match. The leakage magnetic flux densities are inconsequential in the windings and free space in the air, which are 6.42 mT around the edges of the windings and 5.48 mT close to the cores. The EMI caused by the leakage magnetic fluxes is in compliance with the electromagnetic compatibility standards CISPR 11 and IEC 61000-6-3/4/8. Table 8 provides a summary of the maximum magnetic flux densities at different positions.

Table 8. Maximum magnetic flux densities at different positions.

Maximum Flux Density in Ferrite Cores	Maximum Leakage Flux Density in Windings	Maximum Leakage Flux Density in Air
0.33604 T	6.42 mT	5.48 mT

4.3.2. Impedance and Waveform Response Testing Results

The prototype I-SiC-HFT, whose side and top views are shown in Figure 16, has an overall diameter of 94 mm and an overall height of 41 mm. The prototype I-SiC-HFT was built in two winding structures: separated and interleaved, as shown in Figure 17.

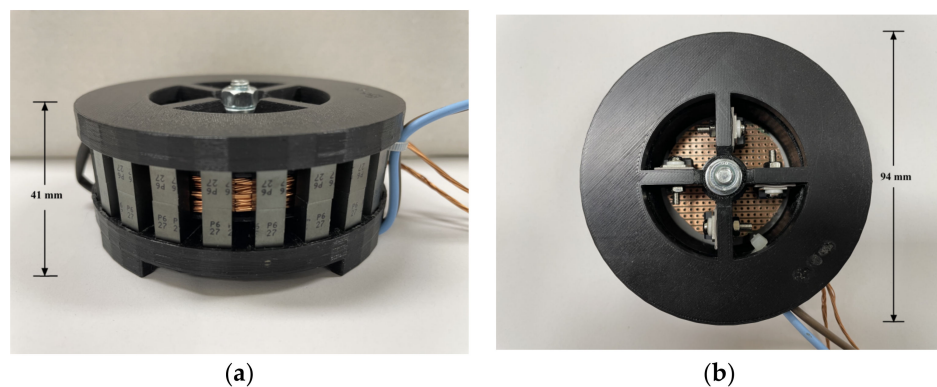


Figure 16. Physical structure of the prototype I-SiC-HFT. (a) Side view (b) Top view.

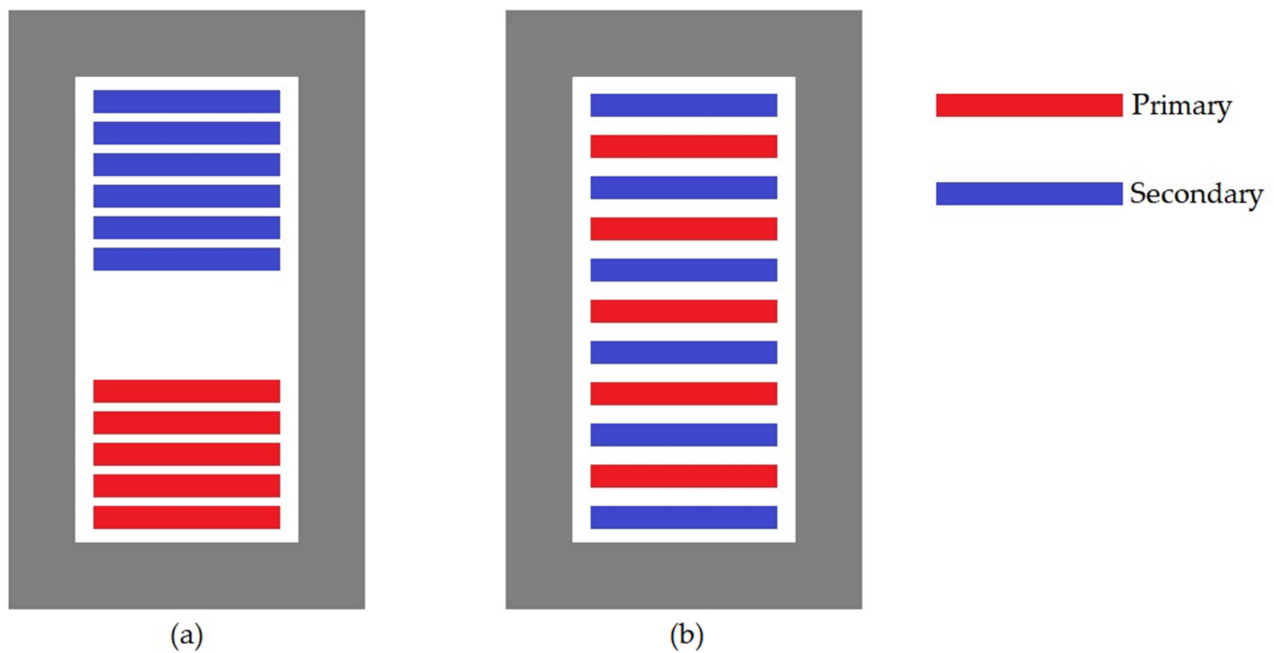


Figure 17. Schematic of two different winding structures: (a) Separated; (b) Interleaved.

The prototype HF transformer with separate and interleaved winding structures underwent impedance testing at various frequencies from 10 kHz to 200 kHz using an R&S[®] HM8118 LCR meter with an HZ186 four-terminal transformer test fixture. Table 9 provides a summary of impedance testing measurements at 100 kHz, and Table 10 presents the comparison between the measured and simulated circuit inductances of the prototype HF transformer with a separate winding structure. The circuit inductances and interwinding capacitances of both winding structures obtained from impedance testing are shown in Figure 18.

Table 9. Impedance measurements of the prototype HF transformer with separate and interleaved winding structures at 100 kHz.

Winding	Test Item	Primary	Secondary	
Separate	Open-circuit test	R_p (k Ω)	159.71	173.77
		L_p (μ H)	235.41	339.08
	Short-circuit test	R_s (m Ω)	301.81	439.10
		L_s (μ H)	5.9862	8.4830
	Interwinding capacitance		22.488 pF	
	Turns ratio		1.20	
	Phase difference		+0.1144 $^\circ$	
	Mutual inductance		281.47 μ H	
	Coupling coefficient		0.996	
Interleaved	Open-circuit test	R_p (k Ω)	142.90	155.56
		L_p (μ H)	242.48	349.46
	Short-circuit test	R_s (m Ω)	125.94	173.03
		L_s (μ H)	1.6567	2.4290
	Interwinding capacitance		169.28 pF	
	Turns ratio		1.20	
	Phase difference		+0.0788 $^\circ$	
	Mutual inductance		290.54 μ H	
	Coupling coefficient		0.998	

Table 10. Comparison between simulated and measured circuit inductances of separate-winding prototype HF transformer.

Circuit Inductance	Simulated	Measured	Difference
Mutual	281.51 μH	281.47 μH	0.02%
Primary leakage	5.7404 μH	5.9862 μH	4.2%
Secondary leakage	8.2660 μH	8.4830 μH	2.6%

Mutual and leakage inductances and interwinding capacitance at various frequencies

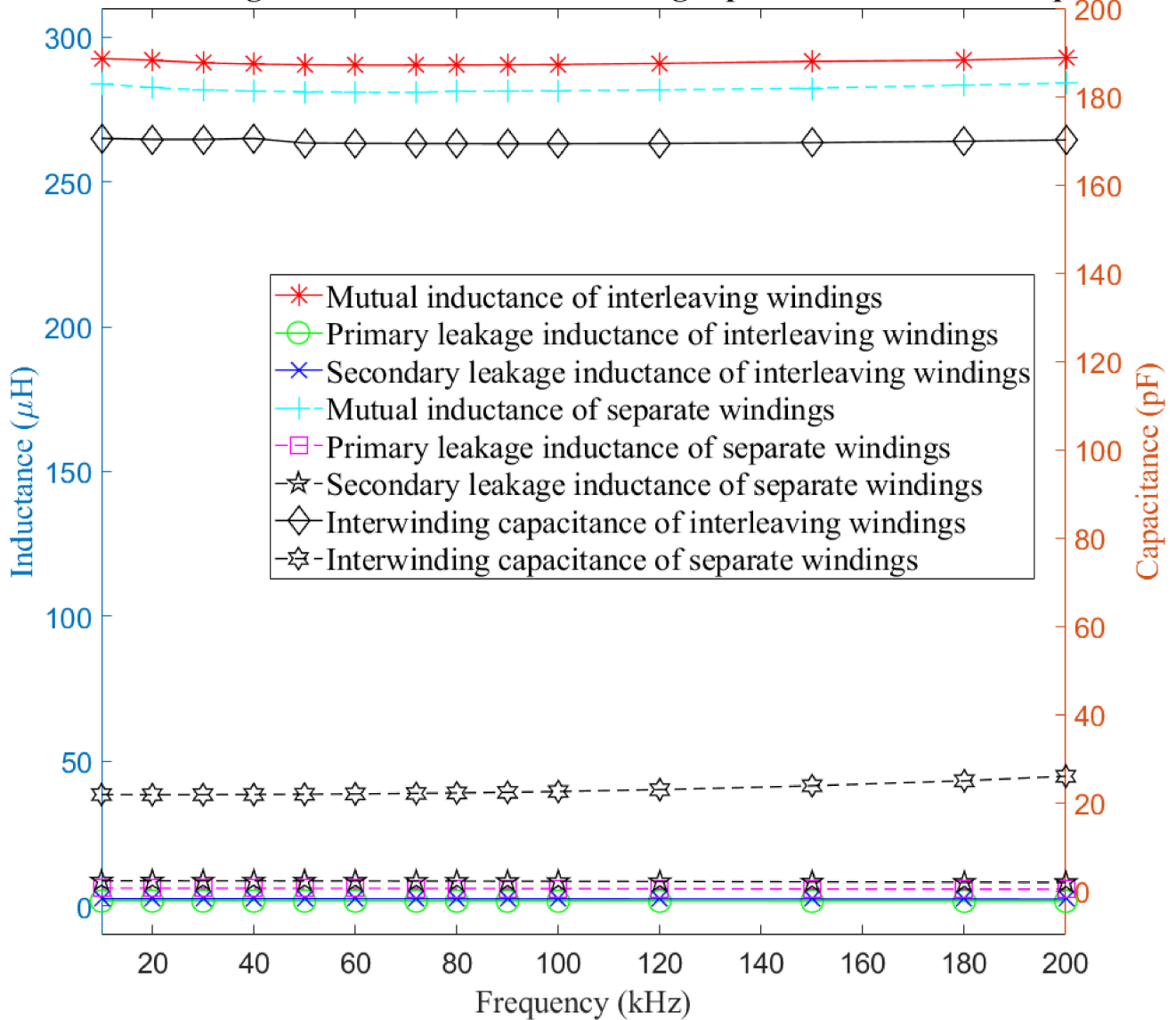


Figure 18. Circuit inductances and interwinding capacitances of separate and interleaved winding structures from 10 to 200 kHz.

The prototype HF transformer shows excellent results in impedance testing as the total leakage inductances are less than 6% and 2% of the mutual inductances for separate and interleaved winding structures respectively, and the interwinding capacitances are in the low picofarad range as well as the phase differences between the primary and secondary windings are negligible for both winding structures. The resistances of the separate windings are higher than those of the interleaved windings because of the larger proximity effect. The circuit inductances and interwinding capacitances of the prototype

HF transformer demonstrate minor variations within well-defined limits for both winding structures, which are expected because they are independent of frequency. From the measurements for the separate winding structure, the turns ratio and inductances of the prototype HF transformer match its simulated voltage ratio and inductances respectively.

The prototype I-SiC-HFT underwent waveform response testing with sinusoidal and square-wave excitations at various frequencies from 50 to 150 kHz. The waveforms of the prototype HF transformer as a separate component and the complete prototype as a system show no distortion for sinusoidal excitation. However, their square-wave waveform responses have some high and narrow voltage spikes that are due to the hard switching of the FB circuitry and small leakage inductance and parasitic capacitance of the HF transformer. Apart from the voltage spikes, the input and output voltages of the prototype I-SiC-HFT are in the correct temporal alignment. Figures 19 and 20 show the waveform responses for excitations of both the prototype HF transformer and the prototype I-SiC-HFT, respectively.

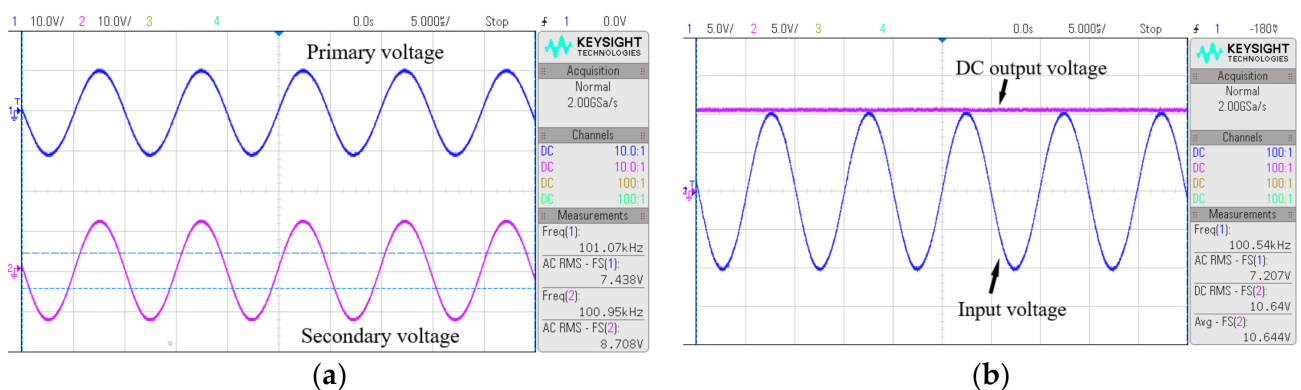


Figure 19. Waveform responses of the HF transformer: (a) Sinusoidal excitation; (b) Square-wave excitation.

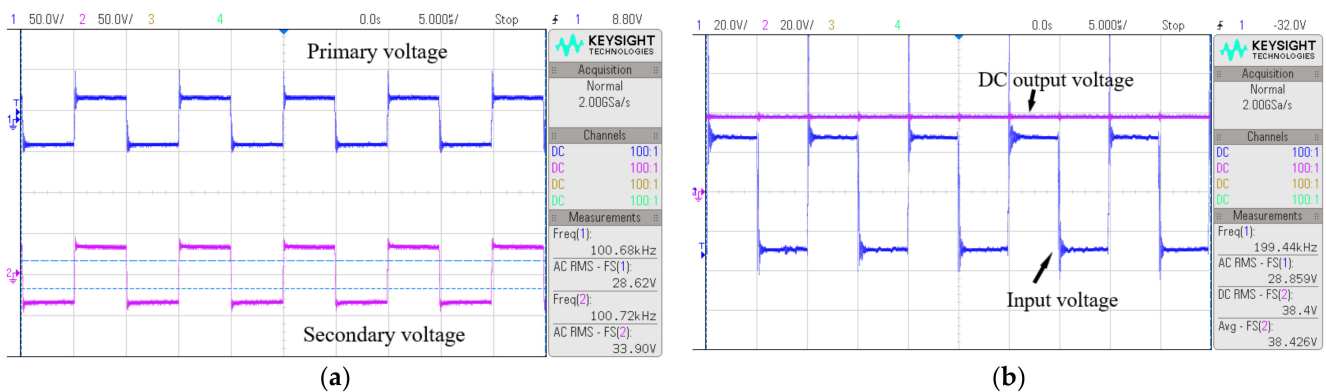


Figure 20. Waveform responses of the I-SiC-HFT: (a) Sinusoidal excitation; (b) Square-wave excitation.

4.3.3. PSIM Power Converter Simulation Results

The PSIM simulation running at the full-load conditions was based on the measured parameters of the prototype I-SiC-HFT, and the data from the datasheets of the Transphorm inverter TDINV3000W050-KIT and SiC Schottky diode S3D06065. Figures 21 and 22 show the simulation circuit diagram and the simulation results respectively. The key simulated results are summarized in Table 11. The prototype transformer as a separate component, the prototype SiC-Schottky-diode-integrated HF AC–DC converter, and the whole system achieved efficiencies of 99.57%, 93.62%, and 90.11%, respectively, for hard switching under full-load conditions.

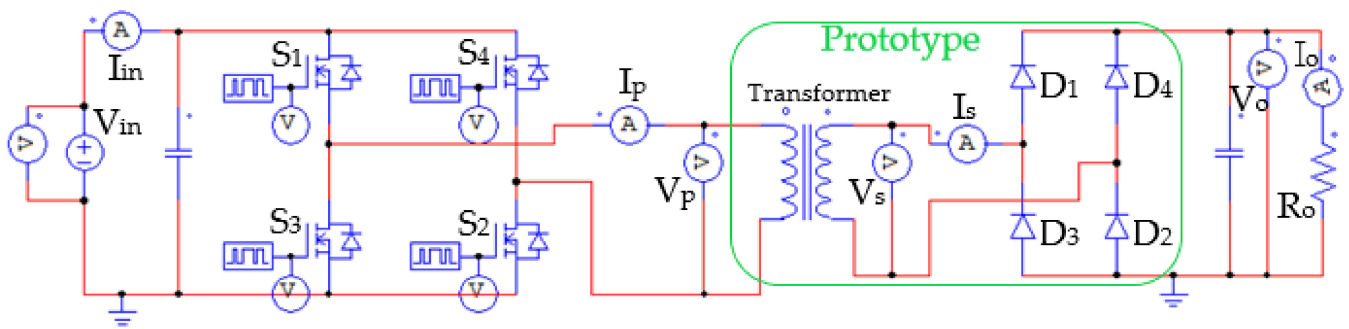


Figure 21. Simulation circuit diagram of the DC–DC system.

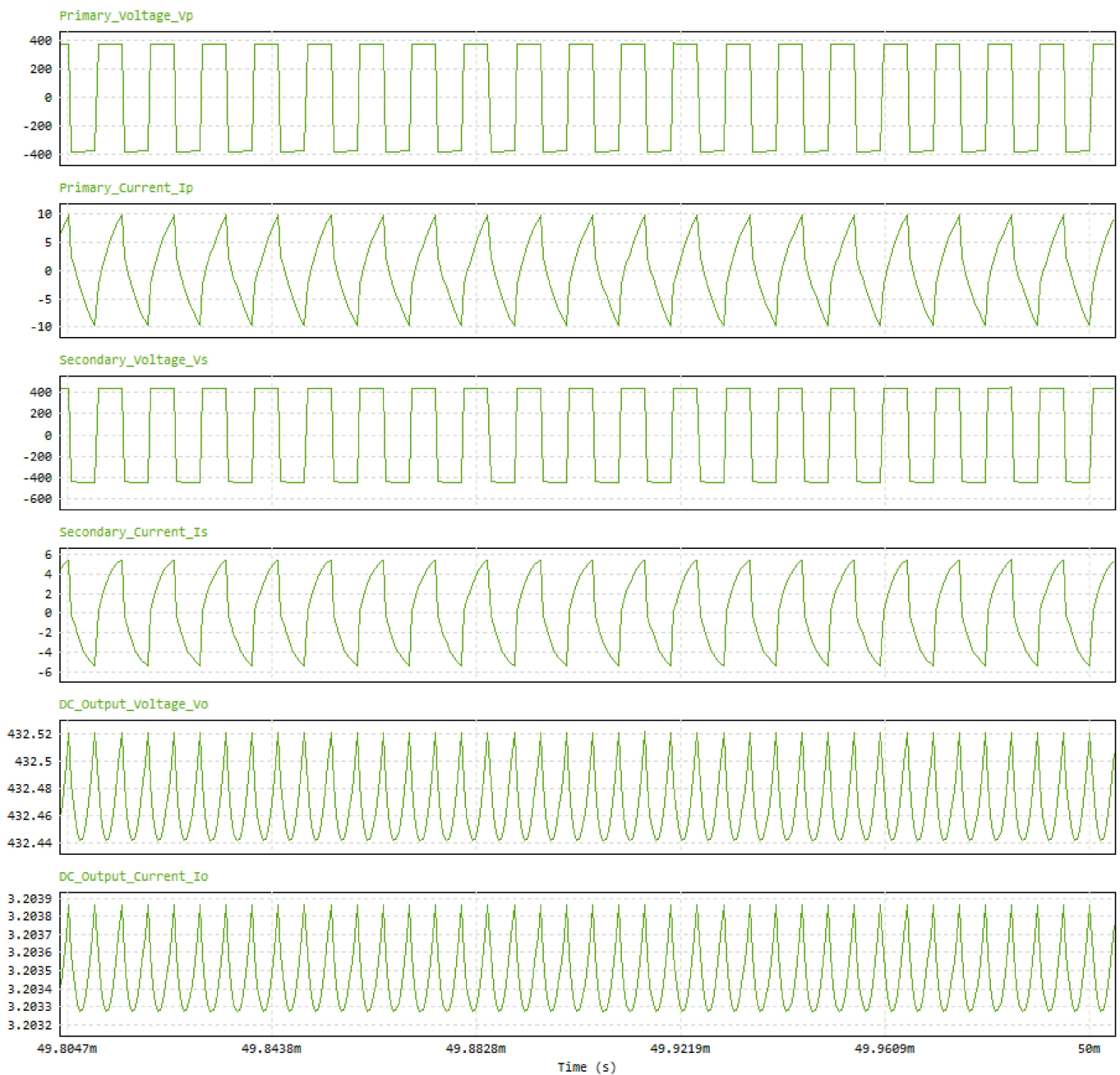


Figure 22. Simulation results of the DC–DC system.

Table 11. Simulation results of the hard-switching DC–DC converter.

Parameter	DC Source	Transformer Primary Side	Transformer Secondary Side	DC Output	Transformer Efficiency	Prototype I-SiC-HFT Efficiency	Overall Efficiency
Voltage	375 V	370.9 V	439.1 V	432.47 V			
Current	4.10 A	3.99 A	3.356 A	3.2035 A	99.57%	93.62%	90.11%
Power	1537.5 W	1479.891 W	1473.6196 W	1385.4176 W			

5. Conclusions

This paper presented a novel structure of an integrated SiC-device within an HF transformer for the PSFB converter, LLC resonant converter, bidirectional PSFB converter, and bidirectional CLLC resonant converter. The design considerations and method of I-SiC-HFT were proposed for determining the HF magnetic structure using distributed ferrite cores and optimising the central space and thermal management for SiC semiconductor devices including SiC MOSFETs, Schottky diodes, and MOSFET modules. This highly compact I-SiC-HFT can achieve volume reduction with high power density and efficiency greater than 98%. The thermal management of SiC devices within I-SiC-HFTs and using the proposed heatsink structure was presented.

The wide power ranges, from 1 kW to 300 kW at the switching frequency and from 50 kHz to 300 kHz for a single module, can be achieved by using the same design methodology. Finally, a small-scale 1.5kW prototype I-SiC-HFT with a power density of 6 kW/L was used to demonstrate the basic structure and to verify the concept through the FEM-based electromagnetic simulation and experiments. The proposed HF transformer does not cause any inductive EMI issue for the SiC devices because the leakage inductance in the air is negligible based on the COMSOL simulation results. The experimental results from the prototype I-SiC-HFT prove that the integration of SiC Schottky diodes into the HF transformer produces a fully functional isolated HF AC–DC power converter with reduced size because there is no need for an AC–DC conversion circuit outside the transformer package. In addition, the DC–DC test system for the prototype I-SiC-HFT will have much higher efficiency with soft-switching techniques.

Author Contributions: All authors contributed to this work. Conceptualization, J.L., F.T. and W.Y.; methodology, J.L., F.T. and W.Y.; software simulation, W.Y.; experimental testing, W.Y. and J.L.; validation, W.Y. and J.L.; formal analysis, W.Y. and J.L.; investigation, W.Y. and J.L.; writing—original draft preparation, W.Y., J.L. and F.T.; writing—review and editing, J.L., F.T., F.B. and A.S.; visualization, W.Y., J.L., F.T., F.B. and A.S.; supervision, J.L., F.T., F.B. and A.S.; project administration, J.L., F.T., F.B. and A.S. All authors have read and agreed to the published version of the manuscript.

Funding: This research received no external funding.

Data Availability Statement: Data are not available on a publicly accessible repository, and they cannot be shared under request.

Acknowledgments: This work was supported by the Australian Research Council Discovery Project under Grant DP180100470 and Griffith University's patent support for PCT international application (No. 17/924,055). We sincerely thank Frank Cole, Gavin McIntosh, Tania Parveen, and Miles Cornish for their contributions to this project.

Conflicts of Interest: The authors declare no conflict of interest.

References

- Guo, Z.; Sha, D. Introduction. In *New Topologies and Modulation Schemes for Soft-Switching Isolated DC–DC Converters*; Chen, W., Chen, Y., He, X., Li, Y., Liu, J., Luo, A., Ma, X., Ruan, X., Eds.; CPSS Power Electronics Series; Springer: Singapore, 2020; pp. 1–16.
- Baars, N.H.; Everts, J.; Huisman, H.; Duarte, J.L.; Lomonova, E.A. A 80-kW Isolated DC–DC Converter for Railway Applications. *IEEE Trans. Power Electron.* **2015**, *30*, 6639–6647. [[CrossRef](#)]
- Xue, F.; Yu, R.; Huang, A.Q. A 98.3% Efficient GaN Isolated Bidirectional DC–DC Converter for DC Microgrid Energy Storage System Applications. *IEEE Trans. Ind. Electron.* **2017**, *64*, 9094–9103. [[CrossRef](#)]

4. Inoue, S.; Akagi, H. A Bidirectional Isolated DC–DC Converter as a Core Circuit of the Next-Generation Medium-Voltage Power Conversion System. *IEEE Trans. Power Electron.* **2007**, *22*, 535–542. [[CrossRef](#)]
5. Nabih, A.; Gadelrab, R.; Prakash, P.R.; Li, Q.; Lee, F.C. High Power Density 1 MHz 3 kW 400 V–48 V LLC Converter for Datacenters with improved Core Loss and Termination Loss. In Proceedings of the 2021 IEEE Applied Power Electronics Conference and Exposition (APEC), Phoenix, AZ, USA, 14–17 June 2021; pp. 304–309.
6. Planar Transformers Family. Available online: <https://www.paytongroup.com/planar-transformers> (accessed on 5 November 2022).
7. Planar Magnetics | Introduction. Available online: <https://standxelectronics.com/products/planar-magnetics/> (accessed on 5 November 2022).
8. HiMAG PLANAR. Available online: <https://www.himag.co.uk/> (accessed on 5 November 2022).
9. 600 kW XM3 High Performance Dual Three-Phase Inverter. Available online: <https://www.wolfspeed.com/crd600da12e-xm3/> (accessed on 5 November 2022).
10. Discrete Silicon Carbide MOSFETs. Available online: <https://www.wolfspeed.com/products/power/sic-mosfets/> (accessed on 5 November 2022).
11. Silicon Carbide Power Modules. Available online: <https://www.wolfspeed.com/products/power/sic-power-modules/> (accessed on 5 November 2022).
12. ON Semiconductor Corporation. The Difference Between GaN and SiC Transistors. *Power Electron. News* **2020**, 1–6.
13. SiC Solutions for DC Fast Charging. Available online: <https://www.wolfspeed.com/knowledge-center/article/designing-with-silicon-carbide-sic-in-electric-vehicle-dc-fast-chargers/> (accessed on 30 June 2022).
14. 11 kW bi-Directional CLLC DC-DC converter with 1200 V and 1700 V CoolSiC™ MOSFETs. Available online: https://www.infineon.com/dgdl/Infineon-UG-2020-31_REF_DAB11KIZSICSYS-UserManual-v01_01-EN.pdf?fileId=5546d46276fb756a0177060f64a829de (accessed on 11 February 2022).
15. PMP21495 6.6 kW, bi-Directional, Dual-Active-Bridge CLLC Resonant Converter Reference Design. Available online: <https://www.ti.com/tool/PMP21495> (accessed on 20 September 2022).
16. De Doncker, R.W.; Divan, D.M.; Kheraluwala, M.H. A three-phase soft-switched high-power-density DC/DC converter for high-power applications. *IEEE Trans. Ind. Appl.* **1991**, *27*, 63–73. [[CrossRef](#)]
17. Tan, N.M.; Abe, T.; Akagi, H. Experimental discussions on operating frequencies of a bidirectional isolated DC-DC converter for a battery energy storage system. In Proceedings of the 2013 IEEE Energy Conversion Congress and Exposition, Denver, CO, USA, 15–19 September 2013; pp. 2333–2340.
18. Tan, N.M.; Abe, T.; Akagi, H. Topology and application of bidirectional isolated dc-dc converters. In Proceedings of the 8th International Conference on Power Electronics-ECCE Asia, Jeju, Republic of Korea, 30 May–3 June 2011; pp. 1039–1046.
19. Akagi, H.; Yamagishi, T.; Tan, N.M.L.; Kinouchi, S.-i.; Miyazaki, Y.; Koyama, M. Power-Loss Breakdown of a 750-V 100-kW 20-kHz Bidirectional Isolated DC–DC Converter Using SiC-MOSFET/SBD Dual Modules. *IEEE Trans. Ind. Appl.* **2015**, *51*, 420–428. [[CrossRef](#)]
20. Deng, C.; Xu, D.; Zhang, Y.; Chen, Y.; Okuma, Y.; Mino, K. Impact of dielectric material on passive integration in LLC resonant converter. In Proceedings of the 2008 IEEE Power Electronics Specialists Conference, Rhodes, Greece, 15–19 June 2008; pp. 269–272.
21. Costa, L.F.; Buticchi, G.; Liserre, M. Highly Efficient and Reliable SiC-Based DC–DC Converter for Smart Transformer. *IEEE Trans. Ind. Electron.* **2017**, *64*, 8383–8392. [[CrossRef](#)]
22. Panda, K.P.; Rout, S. A Cost-Effective Design and Analysis of Full Bridge LLC Resonant Converter. *World Acad. Sci. Eng. Technol. Int. J. Energy Power Eng.* **2016**, *10*, 1143–1150. [[CrossRef](#)]
23. Beiranvand, R.; Rashidian, B.; Zolghadri, M.R.; Alavi, S.M.H. Using LLC Resonant Converter for Designing Wide-Range Voltage Source. *IEEE Trans. Ind. Electron.* **2011**, *58*, 1746–1756. [[CrossRef](#)]
24. Musavi, F.; Craciun, M.; Gautam, D.S.; Eberle, W.; Dunford, W.G. An LLC Resonant DC–DC Converter for Wide Output Voltage Range Battery Charging Applications. *IEEE Trans. Power Electron.* **2013**, *28*, 5437–5445. [[CrossRef](#)]
25. Huang, H. *Designing an LLC Resonant Half-Bridge Power Converter*; Texas Instruments Inc.: Dallas, TX, USA, 2011; pp. 1–27.
26. Abdel-Rahman, S. *Resonant LLC Converter: Operation and Design 250W 33Vin 400Vout Design Example*; Application Note AN 2012-09; Infineon Technologies North America (IFNA) Corp.: Durham, NC, USA, 2012; pp. 1–19.
27. Choi, H. *Design Considerations for an LLC Resonant Converter*; Fairchild Semiconductor: Sunnyvale, CA, USA, 2007; pp. 82–83.
28. Gu, Y.; Hang, L.; Chen, H.; Lu, Z.; Qian, Z.; Li, J. A simple structure of LLC resonant DC-DC converter for multi-output applications. In Proceedings of the Twentieth Annual IEEE Applied Power Electronics Conference and Exposition, APEC 2005, Austin, TX, USA, 6–10 March 2005; pp. 1485–1490.
29. Lu, B.; Liu, W.; Liang, Y.; Lee, F.C.; van Wyk, J.D. Optimal design methodology for LLC resonant converter. In Proceedings of the Twenty-First Annual IEEE Applied Power Electronics Conference and Exposition, APEC'06, Dallas, TX, USA, 19–23 March 2006; pp. 533–538.
30. Adireddy, R.; Pratap, K.N.G.A.; Himaja, T.; Murthy, K.V.S.R. Circuit analysis and modelling of dual active bridge bidirectional converter. *Mater. Today Proc.* **2022**, *56*, 3272–3275. [[CrossRef](#)]

31. Taghizadeh, S.; Hossain, M.J.; Lu, J. Bidirectional isolated vehicle to grid (V2G) system: An optimized implementation and approach. In Proceedings of the 2015 IEEE PES Asia-Pacific Power and Energy Engineering Conference (APPEEC), Brisbane, QLD, Australia, 15–18 November 2015; pp. 1–5.
32. Yade, O.; Gauthier, J.-Y.; Lin-Shi, X.; Gendrin, M.; Zaoui, A. Modulation strategy for a Dual Active Bridge converter using Model Predictive Control. In Proceedings of the 2015 IEEE International Symposium on Predictive Control of Electrical Drives and Power Electronics (PRECEDE), Valparaiso, Chile, 5–6 October 2015; pp. 15–20.
33. Akagi, H.; Kinouchi, S.-i.; Miyazaki, Y. Bidirectional isolated dual-active-bridge (DAB) DC-DC converters using 1.2-kV 400-A SiC-MOSFET dual modules. *CPSS Trans. Power Electron. Appl.* **2016**, *1*, 33–40. [[CrossRef](#)]
34. Alonso, A.R.; Sebastian, J.; Lamar, D.G.; Hernando, M.M.; Vazquez, A. An overall study of a Dual Active Bridge for bidirectional DC/DC conversion. In Proceedings of the 2010 IEEE Energy Conversion Congress and Exposition, Atlanta, GA, USA, 12–16 September 2010; pp. 1129–1135.
35. Singh, R.; Taghizadeh, S.F.; Tan, N.M.L. Battery energy storage system for PV output leveling based on bidirectional isolated DC-DC converter. In Proceedings of the 2013 IEEE Student Conference on Research and Development, Putrajaya, Malaysia, 16–17 December 2013; pp. 84–89.
36. Farooq, Z.; Ullah, N. Single-phase shift control for dual active bridge using adaptive PI control technique. *Int. J. Power Energy Syst.* **2019**, *39*, 148–155. [[CrossRef](#)]
37. Meena, K.; Jayaswal, K.; Palwalia, D.K. Analysis of Dual Active Bridge Converter for Solid State Transformer Application using Single-Phase Shift Control Technique. In Proceedings of the 2020 International Conference on Inventive Computation Technologies (ICICT), Coimbatore, India, 26–28 February 2020; pp. 1–6.
38. Zhao, B.; Yu, Q.; Sun, W. Extended-Phase-Shift Control of Isolated Bidirectional DC-DC Converter for Power Distribution in Microgrid. *IEEE Trans. Power Electron.* **2012**, *27*, 4667–4680. [[CrossRef](#)]
39. Shi, H.; Wen, H.; Chen, J.; Hu, Y.; Jiang, L.; Chen, G.; Ma, J. Minimum-Backflow-Power Scheme of DAB-Based Solid-State Transformer with Extended-Phase-Shift Control. *IEEE Trans. Ind. Appl.* **2018**, *54*, 3483–3496. [[CrossRef](#)]
40. Oggier, G.G.; García, G.O.; Oliva, A.R. Switching Control Strategy to Minimize Dual Active Bridge Converter Losses. *IEEE Trans. Power Electron.* **2009**, *24*, 1826–1838. [[CrossRef](#)]
41. Oggier, G.G.; García, G.O.; Oliva, A.R. Modulation strategy to operate the dual active bridge DC-DC converter under soft switching in the whole operating range. *IEEE Trans. Power Electron.* **2011**, *26*, 1228–1236. [[CrossRef](#)]
42. Zhao, B.; Song, Q.; Liu, W. Efficiency Characterization and Optimization of Isolated Bidirectional DC-DC Converter Based on Dual-Phase-Shift Control for DC Distribution Application. *IEEE Trans. Power Electron.* **2013**, *28*, 1711–1727. [[CrossRef](#)]
43. Zhao, B.; Song, Q.; Liu, W.; Sun, W. Current-Stress-Optimized Switching Strategy of Isolated Bidirectional DC-DC Converter with Dual-Phase-Shift Control. *IEEE Trans. Ind. Electron.* **2013**, *60*, 4458–4467. [[CrossRef](#)]
44. Feng, B.; Wang, Y.; Man, J. A novel dual-phase-shift control strategy for dual-active-bridge DC-DC converter. In Proceedings of the IECON 2014—40th Annual Conference of the IEEE Industrial Electronics Society, Dallas, TX, USA, 29 October–1 November 2014; pp. 4140–4145.
45. Bai, H.; Mi, C. Eliminate Reactive Power and Increase System Efficiency of Isolated Bidirectional Dual-Active-Bridge DC-DC Converters Using Novel Dual-Phase-Shift Control. *IEEE Trans. Power Electron.* **2008**, *23*, 2905–2914. [[CrossRef](#)]
46. Calderon, C.; Barrado, A.; Rodriguez, A.; Alou, P.; Lazaro, A.; Fernandez, C.; Zumel, P. General Analysis of Switching Modes in a Dual Active Bridge with Triple Phase Shift Modulation. *Energies* **2018**, *11*, 2419. [[CrossRef](#)]
47. Wen, H.; Xiao, W. Bidirectional dual-active-bridge DC-DC converter with triple-phase-shift control. In Proceedings of the 2013 Twenty-Eighth Annual IEEE Applied Power Electronics Conference and Exposition (APEC), Long Beach, CA, USA, 17–21 March 2013; pp. 1972–1978.
48. Harrye, Y.A.; Ahmed, K.H.; Adam, G.P.; Aboushady, A.A. Comprehensive steady state analysis of bidirectional dual active bridge DC/DC converter using triple phase shift control. In Proceedings of the 2014 IEEE 23rd International Symposium on Industrial Electronics (ISIE), Istanbul, Turkey, 1–4 June 2014; pp. 437–442.
49. Huang, J.; Wang, Y.; Gao, Y.; Lei, W.; Li, Y. Unified PWM control to minimize conduction losses under ZVS in the whole operating range of dual active bridge converters. In Proceedings of the 2013 Twenty-Eighth Annual IEEE Applied Power Electronics Conference and Exposition (APEC), Long Beach, CA, USA, 17–21 March 2013; pp. 2016–2022.
50. Kumar, A.; Bhat, A.H.; Agarwal, P. Comparative analysis of dual active bridge isolated DC to DC converter with double phase shift and triple phase shift control techniques. In Proceedings of the 2017 Recent Developments in Control, Automation & Power Engineering (RDCAPE), Noida, India, 26–27 October 2017; pp. 257–262.
51. Jung, J.-H.; Kim, H.-S.; Ryu, M.-H.; Baek, J.-W. Design Methodology of Bidirectional CLLC Resonant Converter for High-Frequency Isolation of DC Distribution Systems. *IEEE Trans. Power Electron.* **2013**, *28*, 1741–1755. [[CrossRef](#)]
52. Rezayati, M.; Tahami, F.; Schanen, J.-L.; Sarrazin, B. Generalized State-Plane Analysis of Bidirectional CLLC Resonant Converter. *IEEE Trans. Power Electron.* **2022**, *37*, 5773–5785. [[CrossRef](#)]
53. Zhao, B.; Zhang, X.; Hunag, J. Design of CLLC Resonant Converters for the Hybrid AC/DC Microgrid Applications. In Proceedings of the 2018 IEEE International Power Electronics and Application Conference and Exposition (PEAC), Shenzhen, China, 4–7 November 2018; pp. 1–5.

54. Zahid, Z.U.; Dalala, Z.M.; Chen, R.; Chen, B.; Lai, J.-S. Design of Bidirectional DC–DC Resonant Converter for Vehicle-to-Grid (V2G) Applications. *IEEE Trans. Transp. Electrification*. **2015**, *1*, 232–244. [[CrossRef](#)]
55. Hunag, J.; Zhang, X.; Shuai, Z.; Zhang, X.; Wang, P.; Koh, L.H.; Xiao, J.; Tong, X. Robust Circuit Parameters Design for the CLLC-Type DC Transformer in the Hybrid AC–DC Microgrid. *IEEE Trans. Ind. Electron.* **2019**, *66*, 1906–1918. [[CrossRef](#)]
56. Zou, S.; Lu, J.; Mallik, A.; Khaligh, A. Bi-Directional CLLC Converter with Synchronous Rectification for Plug-In Electric Vehicles. *IEEE Trans. Ind. Appl.* **2018**, *54*, 998–1005. [[CrossRef](#)]
57. Liu, G.; Li, D.; Zhang, J.Q.; Hu, B.; Jia, M.L. Bidirectional CLLC resonant DC-DC converter with integrated magnetic for OBCM application. In Proceedings of the 2015 IEEE International Conference on Industrial Technology (ICIT), Seville, Spain, 17–19 March 2015; pp. 946–951.
58. Bahmani, M.A.; Thiringer, T.; Rabiei, A.; Abdulahovic, T. Comparative Study of a Multi-MW High-Power Density DC Transformer with an Optimized High-Frequency Magnetics in All-DC Offshore Wind Farm. *IEEE Trans. Power Deliv.* **2016**, *31*, 857–866. [[CrossRef](#)]
59. Bahmani, M.A.; Agheb, E.; Thiringer, T.; Høidalen, H.K.; Serdyuk, Y. Core loss behavior in high frequency high power transformers—I: Effect of core topology. *J. Renew. Sustain. Energy* **2012**, *4*, 033112. [[CrossRef](#)]
60. Shamshuddin, M.A.; Rojas, F.; Cardenas, R.; Pereda, J.; Diaz, M.; Kennel, R. Solid State Transformers: Concepts, Classification, and Control. *Energies* **2020**, *13*, 2319. [[CrossRef](#)]
61. Ortiz, G.; Biela, J.; Bortis, D.; Kolar, J.W. 1 Megawatt, 20 kHz, Isolated, bidirectional 12 kV to 1.2 kV DC-DC converter for renewable energy applications. In Proceedings of the International Power Electronics Conference, Sapporo, Japan, 21–24 June 2010; pp. 3212–3219.
62. Villar, I.; Garcia-Bediaga, A.; Viscarret, U.; Etxeberria-Otadui, I.; Rufer, A. Proposal and validation of medium-frequency power transformer design methodology. In Proceedings of the 2011 IEEE Energy Conversion Congress and Exposition, Phoenix, AZ, USA, 17–22 September 2011; pp. 3792–3799.
63. Water, W.; Lu, J. Shielding Analysis of High-Frequency Coaxial Transformers Used for Electric Vehicle On-Board Charging Systems. *IEEE Trans. Magn.* **2013**, *49*, 4005–4008. [[CrossRef](#)]
64. Lu, J.; Dawson, F. Characterizations of High Frequency Planar Transformer with a Novel Comb-Shaped Shield. *IEEE Trans. Magn.* **2011**, *47*, 4493–4496. [[CrossRef](#)]
65. Water, W.; Lu, J. Improved High-Frequency Planar Transformer for Line Level Control (LLC) Resonant Converters. *IEEE Magn. Lett.* **2013**, *4*, 6500204. [[CrossRef](#)]
66. Erickson, R.W.; Maksimović, D. *Fundamentals of Power Electronics*, 3rd ed.; Springer: Cham, Switzerland, 2020; pp. 426–443.
67. McLyman, C.W.T. *Transformer and Inductor Design Handbook*, 4th ed.; CRC Press: Boca Raton, FL, USA, 2011; pp. 4-1–4-42.
68. Yao, W.; Parveen, T.; Lu, J.; Seagar, A. Modular High-Frequency High-Power Transformers for Offshore Wind Turbines. In Proceedings of the 2021 IEEE PES Innovative Smart Grid Technologies—Asia (ISGT Asia), Brisbane, Australia, 5–8 December 2021; pp. 1–5.
69. Barrios, E.L.; Urtasun, A.; Ursúa, A.; Marroyo, L.; Sanchis, P. High-Frequency Power Transformers with Foil Windings: Maximum Interleaving and Optimal Design. *IEEE Trans. Power Electron.* **2015**, *30*, 5712–5723. [[CrossRef](#)]
70. Zhao, B.; Ouyang, Z.; Duffy, M.C.; Andersen, M.A.E.; Hurley, W.G. An Improved Partially Interleaved Transformer Structure for High-Voltage High-Frequency Multiple-Output Applications. *IEEE Trans. Ind. Electron.* **2019**, *66*, 2691–2702. [[CrossRef](#)]
71. Bowen, D.; Lee, A.; Krafft, C.; Mayergoyz, I.D. Design Control of Performance in Nested and Interleaved Winding Printed Circuit Board Transformers for Ethernet Applications. *IEEE Trans. Magn.* **2013**, *49*, 4013–4016. [[CrossRef](#)]
72. Chen, B. Analysis of Effect of Winding Interleaving on Leakage Inductance and Winding Loss of High Frequency Transformers. *J. Electr. Eng. Technol.* **2019**, *14*, 1211–1221. [[CrossRef](#)]
73. Venugopal, A.; Robert, F. Analysis of a Non-overlapping Interleaved Planar Transformer Winding Structure with Reduced Parasitic Effects. *Iran. J. Sci. Technol. Trans. Electr. Eng.* **2022**, *46*, 689–700. [[CrossRef](#)]
74. Petrescu, M.C.; Petrescu, L.; Cazacu, E. Influence of Planar Transformer Windings Interleaving on Parasitic Parameters. *Electroteh. Electron. Autom.* **2018**, *66*, 45–50.
75. Shimura, K.; Tanaka, M.; Satou, M.; Mizuno, T. Copper Loss Reduction in Planar Transformer for LLC Resonant Converter Using Interleaved Winding. *J. Jpn. Soc. Appl. Electromagn. Mech.* **2020**, *28*, 128–133. [[CrossRef](#)]
76. Otsu, S.; Nakamura, K. Characteristics of DC-DC Converter using High-Frequency Amorphous Transformer with Interleaved-Winding for HVDC Transmission System. *Trans. Magn. Soc. Jpn. Spec. Issues* **2020**, *4*, 81–85. [[CrossRef](#)]
77. Zhu, B. The Electromagnetic Compatibility Problems of Integrated Circuits. Ph.D. Thesis, Griffith University, Brisbane, Australia, 2011.
78. Wu, Y.; Yin, S.; Liu, Z.; Li, H.; See, K.Y. Experimental Investigation on Electromagnetic Interference (EMI) in Motor Drive Using Silicon Carbide (SiC) MOSFET. In Proceedings of the 2020 International Symposium on Electromagnetic Compatibility-EMC EUROPE, Rome, Italy, 23–25 September 2020; pp. 1–6.
79. Wu, Y.; Zhang, H.; Yin, S.; Lin, S.; Jiang, T.; Bi, C.; Li, H.; Cheng, Y. Investigation of Conducted Electromagnetic Interference of Three-Level SiC Power Module. In Proceedings of the 2022 Asia-Pacific International Symposium on Electromagnetic Compatibility (APEMC), Beijing, China, 1–4 September 2022; pp. 698–701.

80. Ma, W.; Wu, Y.; Li, H.; Chu, D. Investigation of the Gate Resistance and the RC snubbers on the EMI Suppression in Applying of the SiC MOSFET. In Proceedings of the 2019 IEEE International Conference on Mechatronics and Automation (ICMA), Tianjin, China, 4–7 August 2019; pp. 2224–2228.
81. Zheng, L.; Han, X.; An, Z.; Kandula, R.P.; Kandasamy, K.; Saeedifard, M.; Divan, D. SiC-Based 5-kV Universal Modular Soft-Switching Solid-State Transformer (M-S4T) for Medium-Voltage DC Microgrids and Distribution Grids. *IEEE Trans. Power Electron.* **2021**, *36*, 11326–11343. [[CrossRef](#)]

Disclaimer/Publisher’s Note: The statements, opinions and data contained in all publications are solely those of the individual author(s) and contributor(s) and not of MDPI and/or the editor(s). MDPI and/or the editor(s) disclaim responsibility for any injury to people or property resulting from any ideas, methods, instructions or products referred to in the content.